sustainability

MDPI

Article

Next-Generation Sustainable Adobe Materials: Multifunctional Coatings Based on $LaFeO_3$ Nanoparticles and Hydro- and Oleo-Repellent Formulations

Víctor M. Tena-Santafé [1], Loucas Kyriakou [1], Gurbir Kaur [1,2], José M. Fernández [1], Íñigo Navarro-Blasco [1] and José I. Álvarez [1,*]

[1] Materials and Cultural Heritage (MATCH) Group, Department of Chemistry, University of Navarra, Navarra, 31008 Pamplona, Spain; vmtena@unav.es (V.M.T.-S.); lkyriakou@unav.es (L.K.); gkaur@external.unav.es or gurbir.kaur@thapar.edu (G.K.); jmfdez@unav.es (J.M.F.); inavarro@unav.es (Í.N.-B.)

[2] Department of Civil Engineering, Thapar Institute of Engineering and Technology, Patiala 147004, Punjab, India

* Correspondence: jalvarez@unav.es

Abstract

Adobe is a sustainable yet highly porous construction material, inherently vulnerable to moisture and environmental pollution, which poses challenges for both contemporary construction and heritage conservation. This study presents multifunctional coatings that combine hydrophobic/oleophobic and photocatalytic properties to enhance adobe durability. The coatings incorporate nano-heterostructured $LaFeO_3$ photocatalysts into water-repellent and hydro-oleo-repellent formulations, selected to preserve the characteristic dark brown color of adobe. Microstructural analyses revealed the formation of non-uniform protective layers, particularly in hydro-oleo-repellent systems, which influenced performance. The treated surfaces exhibited significant water and oil repellency, while maintaining adequate vapor permeability. Durability tests confirmed improved resistance to water ingress, reduced capillary absorption, and enhanced erosion resistance compared to untreated adobe. Sustainability assessments highlighted the environmental and economic benefits of the proposed approach, especially when using locally sourced materials. Overall, this work proposes a scalable and multifunctional strategy that integrates protective and photocatalytic functionalities to extend the service life of both historical and modern adobe structures.

Keywords: built heritage; adobe; multifunctional coatings; nanoparticles; $LaFeO_3$; waterproofing; oil repellency

Academic Editor: Antonio Caggiano

Received: 12 March 2026
Revised: 10 April 2026
Accepted: 14 April 2026
Published: 22 April 2026

1. Introduction

Construction activities are closely linked to the economic development of countries. Increase in gross domestic product are typically accompanied by growth in construction activity and, consequently, in environmental pollution [1,2]. Although developed economies may eventually experience a decline in emissions, these reductions do not offset the continued expansion occurring in emerging economies. The cement industry exemplifies this dynamic, as it remains one of the most energy-intensive and pollutant-emitting industrial sectors. Moreover, the COVID-19 pandemic and ongoing geopolitical instability have introduced additional uncertainties regarding the sector's evolution and its role in future reconstruction efforts [3–5].

Within this context, reconciling the construction–cost–pollution trinomial has become increasingly urgent. Raw earth emerges as an abundant, low-cost, low-carbon, and easily processable material that requires minimal industrial infrastructure [6]. These characteristics have renewed interest in earthen construction techniques such as adobe, compressed earth blocks, rammed earth, and soil–cement mortars, whose adoption depends on local needs and climatic conditions [7].

Despite these advantages, earth-based materials still face significant challenges that limit their large-scale implementation. These include variability and inadequacy of local soils, lack of standardized quality control, long construction times, empirical design approaches, high sensitivity to moisture ingress, limited durability, reliance on chemical stabilizers, and uncertainties concerning actual energy efficiency [8–14].

Several strategies have been explored to enhance the performance of earthen materials. Stabilization with ordinary Portland cement (OPC) is among the most widely adopted solutions, as additions of 5–10% OPC can substantially improve mechanical strength, durability, and resistance to water erosion [10]. However, this approach raises compatibility and sustainability concerns, particularly when applied to historical earthen structures. In accordance with restoration principles, favouring compatibility, reversibility, and minimal invasion, protective surface coatings have been investigated as an alternative strategy.

Conventional water-repellent coatings, including waxes, resins, and acrylates, have been extensively applied to porous substrates to limit water ingress [15–21]. Although effective, these materials often present drawbacks such as limited durability, alteration of surface appearance, and insufficient resistance to pollutants or graffiti [22,23]. Consequently, research has shifted toward multifunctional or "smart" coatings that combine water repellency with additional properties, such as biocidal activity, resistance to biological colonization, and photocatalytic self-cleaning capabilities [24–28]. Recent studies have further explored advanced functional coatings with controllable wettability and environmentally responsive features, including switchable wettability systems [29], and sustainable thermochromic coatings [30].

Semiconductor-based nanoparticles, particularly TiO_2 and ZnO, have demonstrated the ability to degrade organic pollutants, reduce microbial growth, and maintain cleaner surfaces through the combined effects of photocatalysis and hydrophobicity [31–33]. In this context, TiO_2 has been extensively studied due to its low toxicity, high compatibility with construction materials, and superior catalytic activity compared to other metal oxides [31–33]. However, it presents certain challenges, including cost, limited absorption of visible sunlight (non-ultraviolet) [32–34], and predominant use in bulk applications rather than coatings. The latter can lead to the loss of photocatalyst within the interior of construction materials, limiting its applicability to new structures and reducing its potential for decontaminating existing buildings.

The composition of photocatalysts can be modified to enhance sensitivity to visible light. For example, the incorporation of ZnO improves photostability, increases the lifetime of electron–hole pairs, and extends photon absorption to longer wavelengths [35,36]. Bismuth oxides have also been studied due to their availability, low cost, low toxicity, good biocompatibility, and potential for doping and cocatalyst formation [37,38]. Their performance can be further enhanced through heterostructure formation, such as TiO_2–ZnO systems [35,36] or Bi_2O_3-ZnO composites [37–39], which broaden light absorption and improve photocatalytic efficiency.

To date, multifunctional coatings of this type have been primarily applied to stone substrates and lime or lime-cement mortars [40–43], showing promising results in terms of durability and surface protection. However, their application to earthen materials, particularly adobe, remains largely unexplored. This gap is notable given adobe's intrinsic

vulnerability to moisture and environmental pollutants, which makes it an ideal candidate for protective treatments. One limiting factor is the risk of surface whitening caused by conventional photocatalysts, which contrasts with the typically dark tones of earthen substrates. This concern has motivated the investigation of alternative photocatalysts such as $LaFeO_3$ nanoparticles, which exhibit photocatalytic activity [44,45] and possess an intrinsic dark-brown coloration that better preserves the original aesthetic appearance.

Although other iron oxides such as Fe_2O_3 and Fe_3O_4 can exhibit photocatalytic activity, Fe_2O_3 suffers from high electron–hole recombination, which limits its efficiency under visible light [46], while Fe_3O_4 requires special conditions or the formation of heterojunctions to behave as a semiconductor, restricting its performance in conventional photocatalytic applications [47]. In contrast, $LaFeO_3$ combines a suitable band gap for visible light absorption with a perovskite structure that promotes charge separation, making it more effective for these processes. Moreover, $LaFeO_3$ exhibits a brown coloration in its pure perovskite form, as has been demonstrated in studies on rare-earth ferrite pigments where its hue ranges from brown to yellow depending on composition, and the base $LaFeO_3$ is brown [48]. In contrast, Fe_2O_3 typically appears reddish-brown colors [49], and Fe_3O_4 is commonly encountered as a black or dark brown/black pigment [50]. These differences in color can be important in heritage conservation contexts, where ensuring compatible chromatic properties of added materials with historical substrates is desirable.

The aim of this work was to evaluate the performance of sustainability-oriented, multifunctional coatings applied to adobe substrates, combining highly water-repellent (W) and water–oil-repellent (O) matrices incorporating $LaFeO_3$ nanoparticles. The microstructure of the coatings was characterized, and their repellency against different liquids was assessed through contact angle measurements and Karsten tube penetration tests. The influence of the coatings on water vapor permeability was also examined, while durability was evaluated using water immersion and Swinburne Accelerated Erosion Tests (SAET). Additionally, the photocatalytic activity of the coatings was investigated to confirm their multifunctional behavior.

Life Cycle Assessment (LCA) and Life Cycle Costing (LCC) analyses were conducted assuming the use of on-site soil for adobe production and accounting for the enhanced durability provided by the coatings. The results indicate that the synergistic combination of photocatalytic activity and hydro-/oleo-repellency substantially improves both durability and surface performance. This approach offers a sustainable and innovative strategy for preserving earthen heritage while promoting environmentally responsible and durable new adobe constructions.

2. Materials and Methods

2.1. Materials

This study investigates adobe substrates treated with multifunctional coatings formulated to provide highly water-repellent and water-oil-repellent properties, incorporating $LaFeO_3$ nanoparticles. An overview of the materials used is presented in Figure 1a.

The adobe specimens were supplied by the Polytechnic University of Catalonia and were produced from excavated soil obtained within the framework of the TerraCycle project. Two commercial carrier media provided by TECNAN (Los Arcos, Navarra, Spain) were used to disperse the photocatalytic nanoparticles at concentrations of 1, 3 and 5% wt/vol. The highly hydrophobic medium was Tecnadis Aquashield Forte (hereafter referred to W-type), while the hydro-oleophobic medium was Tecnadis PRS Performance (hereafter referred to as O-type).

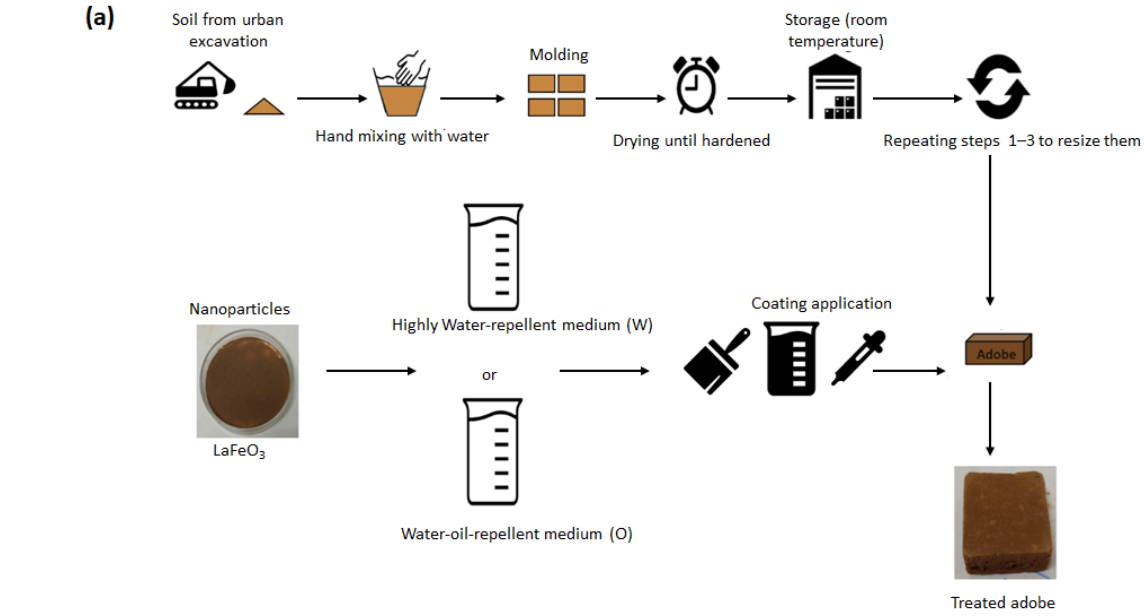

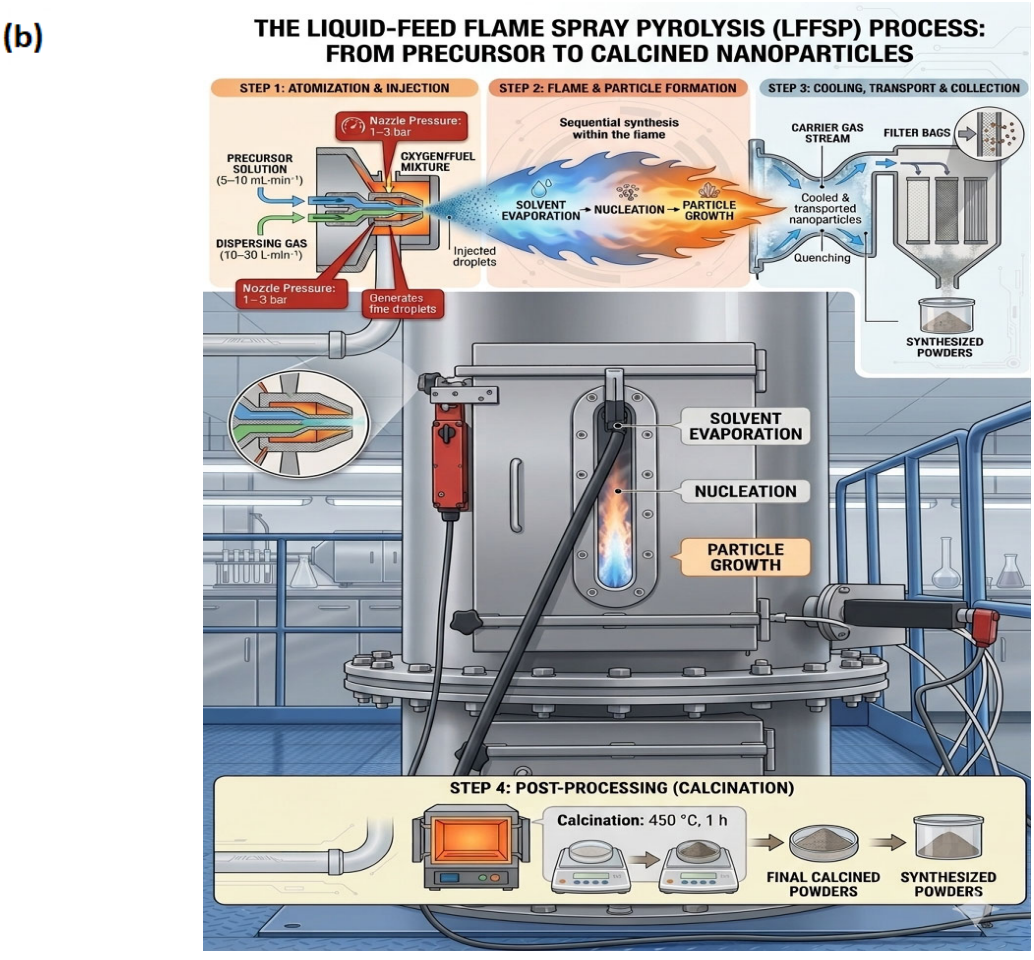

Figure 1. Workflow for the preparation of coatings: (**a**) adobe bricks and coating formulation, and (**b**) Scheme of the liquid-feed flame spray pyrolysis for $LaFeO_3$ synthesis (Image generated using Gemini 3 Flash, Web Version (Google, 16 April 2026) via the following prompt: liquid-feed flame spray pyrolysis for nanoparticles synthesis).

The photocatalyst $LaFeO_3$ was synthesized by Flame Spray Pyrolysis (FSP) at the Lurederra Technological Centre (Los Arcos, Navarra, Spain), and it is hereafter referred to as LaFe for simplicity. The synthesis procedure involved tailoring precursor solutions

to ensure chemical stability and adequate calorific value to complete combustion and nanoparticle formation. The precursors consisted of organometallic compounds (e.g., ethyl hexanoates, acetylacetonates, butoxides, and propoxides) dissolved in solvents such as isopropanol, toluene, xylene, and acetic acid.

The Liquid-Feed Flame Spray Pyrolysis (LFFSP) process involved atomizing the precursor solution using a dispersing gas to generate fine droplets that were injected into the flame. Within the flame, solvent evaporation, nucleation, and particle growth occurred sequentially. A carrier gas stream subsequently cooled and transported the formed nanoparticles, which were collected using filter bags. To ensure the removal of residual organic species and guarantee phase purity, the synthesized powders were calcined at 450 °C for 1 h prior to their incorporation into the coating formulations. Figure 1b showed the process.

2.2. Methods

2.2.1. Characterization of Nanoparticles and Adobe Raw Materials

The chemical composition of the synthesized nanoparticles was determined by X-ray fluorescence (XRF). XRF analyses were performed using a Bruker S2 Puma spectrometer (Bruker, Billerica, MA, USA). The samples were ground, dried, and pressed into pellets using a stearate binder. Measurements were conducted under a helium atmosphere to enhance the detection of light elements, applying an accelerating voltage of 50 kV, a current of 1 mA, and an acquisition time of 300 s per sample. Quantitative analysis was achieved through calibration with certified reference materials. With the aim of determining the mineralogical composition, X-ray diffraction (XRD) patterns were recorded using a Bruker D8 Advance diffractometer (Bruker, Billerica, MA, USA) with Cu Kα1 radiation. Data were collected over a 2θ range of 5–80°, with a step size of 0.03° and an acquisition time of 1 s per step. Phase identification was carried out using Diffrac.EVA V4.3 software (Bruker AXS GmbH, Karlsruhe, Germany) by comparison with reference patterns from the International Centre for Diffraction Data (ICDD, Newtown Square, PA, USA).

To investigate the mineralogical composition of the soils used for adobe production, a classical clay mineral analysis based on oriented aggregate mounts was performed. Powdered samples (passed through a 2 mm sieve) were weighed into Falcon tubes, and 10 mL of a 4% sodium hexametaphosphate solution was added as a dispersant. The suspension was subjected to ultrasonic treatment for 10 min. Water was then added up to 45 mL, and the mixture was homogenized and centrifuged at 750 rpm for 3 min. The supernatant was subsequently extracted and deposited onto three round glass slides. After drying at room temperature under light-protected conditions, the first slide was analyzed by XRD in the 5–40° 2θ range, with a step size of 0.02° and an acquisition time of 1 s per step. The second slide was exposed to ethylene glycol vapor in a desiccator at 60 °C for 24 h. After cooling to room temperature, it was analyzed under the same XRD conditions. The third slide was calcined in a muffle furnace at 500 °C for 1 h, cooled in a desiccator, and subsequently measured under identical XRD conditions. This procedure allowed the identification and differentiation of expandable and non-expandable clay minerals.

Morphological, textural, and compositional features were examined using Transmission Electron Microscopy (TEM) and Scanning Electron Microscopy (SEM). TEM observations were performed with a JEOL JEM-2010 microscope (JEOL Ltd., Tokyo, Japan) operating at 200 keV. Images were acquired using a GATAN ORIUS SC600 camera (Gatan Inc., Pleasanton, CA, USA) and processed with DigitalMicrograph software (Gatan Inc., Pleasanton, CA, USA). SEM images were obtained using a EM-30N microscope (COXEM Co., Ltd., Daejeon, Republic of Korea). Elemental composition was analyzed using a Quantax Compact30 EDS detector (Bruker, Billerica, MA, USA), and data were processed

with Esprit Compact software (Bruker, Billerica, MA, USA). Prior to SEM examination, the powders were sputter-coated with a thin gold layer using a SPT-20 ion sputter coater (COXEM Co., Ltd., Daejeon, Republic of Korea) to improve electrical conductivity.

The specific surface area was determined using the Brunauer–Emmett–Teller (BET) method with a Micromeritics ASAP 2020 analyzer (Micromeritics Instrument Corp., Norcross, GA, USA). Approximately 0.2–0.3 g of sample was degassed under vacuum at 90 °C for 1 h, followed by 200 °C for 4 h, with a heating rate of 10 °C·min^{-1}. Nitrogen adsorption–desorption isotherms were recorded at −196 °C over a relative pressure (P/P_0) range of 0.05–0.3. The BET equation was applied to calculate the specific surface area.

2.2.2. Preparation of the Substrates and Multifunctional Active Coatings

Adobe bricks were prepared by mixing soil with water (adding enough to make the clay workable and moldable) and casting the resulting mud into square molds (5 × 5 × 2 cm). The specimens were then left to cure under ambient conditions for one week. Uncoated samples were designated as C (control). Samples treated with the carrier media were labelled as W-number (highly water-repellent medium) or O-number (oil–water-repellent medium), where the number indicates the number of repeated coating applications. Coated samples containing photocatalytic nanoparticles were labelled using a code that combines the catalyst content (1, 3, or 5% nanoparticles, expressed as photocatalyst weight per volume of suspension), the type of suspension applied (W for highly water-repellent or O for oil–water-repellent), and a final digit indicating the number of consecutive coating applications (1, 2 or 3). The different formulations are summarized in Table 1.

Table 1. Composition and nomenclature of the adobe samples and multifunctional coatings.

Photocatalyst	Samples	Medium
-	C	-
	W-1	Highly water repellent
	W-2	Highly water repellent
	W-3	Highly water repellent
	O-1	Oil and water repellent
	O-2	Oil and water repellent
	O-3	Oil and water repellent
1% LaFe	1% LaFe-W-1	Highly water repellent
	1% LaFe-W-2	Highly water repellent
	1% LaFe-W-3	Highly water repellent
	1% LaFe-O-1	Oil and water repellent
	1% LaFe-O-2	Oil and water repellent
	1% LaFe-O-3	Oil and water repellent
3% LaFe	3% LaFe-W-1	Highly water repellent
	3% LaFe-W-2	Highly water repellent
	3% LaFe-W-3	Highly water repellent
	3% LaFe-O-1	Oil and water repellent
	3% LaFe-O-2	Oil and water repellent
	3% LaFe-O-3	Oil and water repellent

Table 1. *Cont.*

Photocatalyst	Samples	Medium
5% LaFe	5% LaFe-W-1	Highly water repellent
	5% LaFe-W-2	Highly water repellent
	5% LaFe-W-3	Highly water repellent
	5% LaFe-O-1	Oil and water repellent
	5% LaFe-O-2	Oil and water repellent
	5% LaFe-O-3	Oil and water repellent

Prior to application, each suspension was subjected to magnetic stirring for 45 min to ensure proper nanoparticle dispersion. The coatings were then applied to the adobe samples (5 × 5 × 2 cm). Depending on the requirements of the subsequent test, the application was performed either by depositing the suspension using a pipette—ensuring reproducibility of the applied volume—onto samples positioned horizontally, or by immersing the adobe bricks in the suspension for 5–10 s.

A one-hour interval between successive applications was maintained to allow drying of the previous layer. After coating, the specimens were left to rest for 24 h under ambient conditions before characterization. All measurements were performed in triplicate. The particle size distribution of the suspensions was determined by laser diffraction using a Malvern Mastersizer (Malvern Panalytical Ltd., Malvern, UK).

2.2.3. Determination of Coating Thickness and Water and Oil Repellency of Multifunctional Active Coatings

The thickness of the coating layers was measured using a 200 Ultrasonic Coating Thickness Gauge, with an ultrasonic coupling gel supplied by Neurtek (Eibar, Spain).

The water- and oil-repellent properties of the coatings were evaluated by static contact angle measurements and Advancing and Receding Contact Angle (ARCA) tests, carried out on OCA 15EC Dataphysics goniometer (Filderstadt, Germany). Static contact angles were measured to assess both water and oil repellency using 3 µL droplets of water, olive oil, sunflower oil, or hexadecane, dispensed at a controlled rate of 1 µL/s.

Although water and hexadecane are commonly used as reference liquids in contact angle measurements [51], olive and sunflower oils were also included for two main reasons. First, their slightly higher surface tension compared to hexadecane allows better discrimination between the performance of the different coatings. In general, the very low surface tension of hexadecane often leads to rapid absorption by the surface, making reliable comparative measurements difficult. Second, vegetable oils more closely represent the characteristics of fouling agents commonly encountered on building surfaces than hexadecane.

Dynamic contact angle measurements were performed by increasing and subsequently decreasing the droplet volume under controlled conditions. The tests started with an initial droplet of 25 µL, with dispensing and withdrawal rates of 2 µL/s and an equilibration time of 1 s. To ensure measurement reproducibility, the stability of the contact angle was monitored for 10 s. The theoretical background of the Wenzel and Cassie-Baxter wetting models, as well as the definition of superhydrophobic surfaces, has been described elsewhere [39,52].

2.2.4. Determination of Water Vapor Permeability, Water Immersion Durability Test, Karsten Tube Penetration Test and Swinburne Accelerated Erosion Test (SAET)

Water vapor permeability was evaluated according to the standard UNE-EN 15803: 2010 [53]. This test aimed to determine whether the applied coatings maintained adequate vapor permeability. Ideally, protective coatings should allow sufficient breathability of substrate, enabling the passage of water vapor and preventing internal condensation, which may accelerate material degradation.

For this purpose, saturated KCl solutions (10.65 g KCl in 30 mL of water) were prepared. The containers were sealed onto the adobe specimens using silicone to avoid leakage. The coated surface of the sample was oriented toward the solution, maintaining a gap of approximately 2.5 cm between the liquid and the specimen. The complete container-solution-adobe assembly was weighed six times at regular intervals, using 8:00 and 16:00 as reference times. The mathematical procedure used to calculate the relevant permeability parameters is described in the Appendix A. Saturation vapor pressure data for water at the operating temperature were obtained from the National Institute of Standards and Technology (NIST) database [54].

The water immersion test was conducted to evaluate the ability of the coatings to improve the durability of adobe by providing water resistance. Effective coatings should limit water ingress into the substrate, thereby preventing dissolution of components, structural weakening, and eventual specimen disintegration. For this test, individual beakers containing 200 mL of water were prepared for each sample. The specimens were weighed prior to immersion, and once submerged, their mass was recorded at one-minute intervals until structural collapse occurred.

The Karsten tube penetration test [55,56] was used to assess the resistance of the coatings to liquid penetration into the adobe bricks. In addition to water, olive oil and sunflower oil were also used as test liquids. The Karsten tube can be applied in either vertical or horizontal configurations depending on the type of surface being simulated. The horizontal configuration is typically used for vertical surfaces, allowing liquid penetration solely through capillary action without the influence of hydrostatic pressure from the liquid column. This setup simulates the absorption of rainwater or lateral moisture in walls. Conversely, the vertical configuration is used for horizontal surfaces, where the liquid column exerts downward hydrostatic pressure, simulating water penetration on exposed horizontal surfaces.

In the present study, the horizontal configuration was selected, as illustrated in Figure 2, to simulate capillary absorption typical on vertical wall surfaces. The same experimental configuration was applied when testing the oil-based liquids.

The pipettes used in the Karsten tube tests were manufactured by Ludwig Mohren KG. Each device consists of a pipette with a dome of 30 mm in diameter connected to a calibrated tube with a volume scale, where a height of 10 cm corresponds to a 10 m water column. Plasticine, also supplied by Mohren, was used to seal the contact surface between the pipette and the specimen, preventing liquid leakage and ensuring proper adhesion of the device.

A circular test area of approximately 20 mm in diameter (≈3 cm^2) was defined on the sample surface. After filling the pipette with 10 mL of liquid, the decrease in liquid volume was recorded at one-minute intervals for a total duration of 10 min. The volume measured after the tenth minute was interpreted according to standard permeability tables [56].

Since the RILEM Technical Committee TC 25-PEM method is primarily designed for water, an oil–water absorption ratio (R) was calculated according to Equation (1):

$$R = \frac{V_{oil\ 10min}}{V_{water\ 10min}} \quad (1)$$

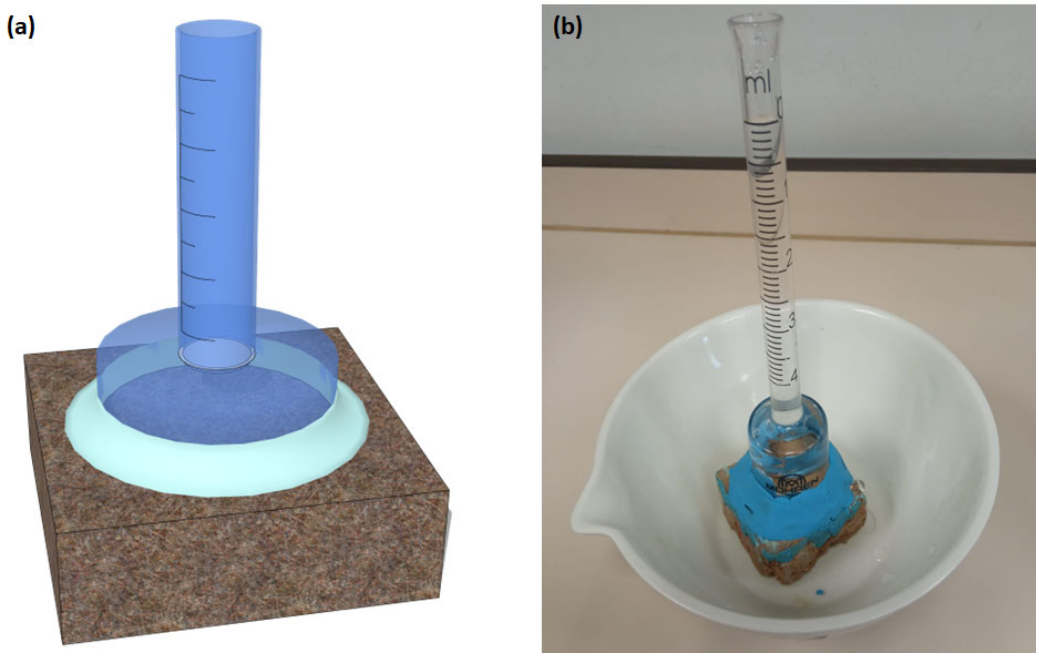

Figure 2. Karsten tube penetration test: (**a**) schematic representation of the experimental setup and (**b**) photograph of the test performed with water.

Values of R = 1 indicate similar absorption rates for oil and water (non-oleophobic behavior), R < 1 indicates reduced oil absorption and therefore oleo repellent behavior, whereas R > 1 indicates preferential oil absorption (oleophilic behavior). This ratio-based approach enables the evaluation of oil permeability by comparison with water permeability data, avoiding the need for dedicated oil permeability reference tables.

Finally, the improvement in the resistance of the adobe bricks to erosion after coating application was evaluated using the Swinburne Accelerated Erosion Test (SAET) [57–59]. In this test, a 250 mL separatory funnel was filled with deionized water and adjusted to deliver a flow rate of 1 drop per second, following the experimental setup illustrated in Figure 3. The outlet tube released droplets with an approximate diameter of 5 mm.

2.2.5. Photocatalytic Activity Evaluation

The photocatalytic performance of the nanoparticles and of the adobe bricks treated with multifunctional coatings was evaluated through NO_x removal experiments carried out in a laminar flow reactor. The test followed the procedure described in ISO 22197-1:2016 [60], which is summarized in Figure 4.

The irradiance of the lamp was reported as 43.4 $W \cdot m^{-2}$ using a Traceable ultraviolet light meter (Control Company, Friendswood, TX, USA; UV-A sensor, 320–390 nm), as reported by Pérez-Nicolás M et al. [61]. At a working distance of 0.5 m, the nominal irradiance values were 41.4 $W \cdot m^{-2}$ in the 780–400 nm range, 13.6 $W \cdot m^{-2}$ in the 400–315 nm range, and 3.0 $W \cdot m^{-2}$ in the 315–280 nm range. Due to the emission of visible, UVA, and UVB radiation, this lamp provides a solar-like spectral distribution.

For the photocatalytic tests, 0.5 g of bare photocatalyst powder was homogeneously distributed over a surface area of 30.1 cm^2, whereas for coated specimens the active surface corresponded to the exposed sample area of 25 cm^2. Photocatalytic efficiency was calculated by comparing the mean NO_x concentration values from recorded during the first 10 min (dark conditions, stabilization phase) with those obtained during the last 10 min of the illumination period.

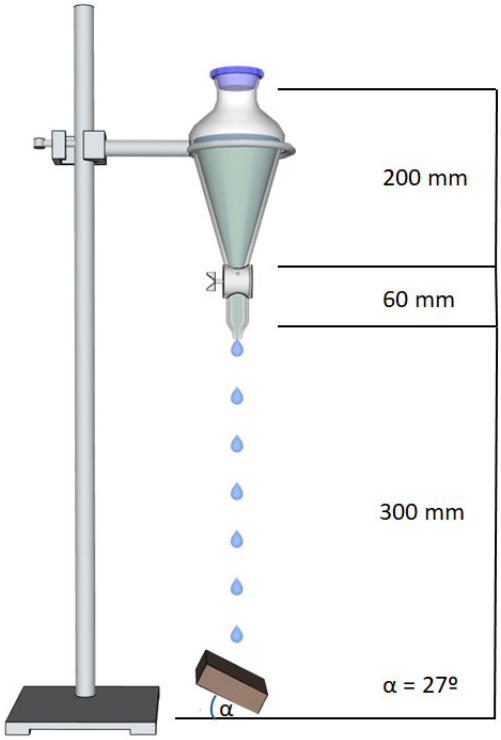

Figure 3. Schematic representation of the Swinburne Accelerated Erosion Test (SAET) setup.

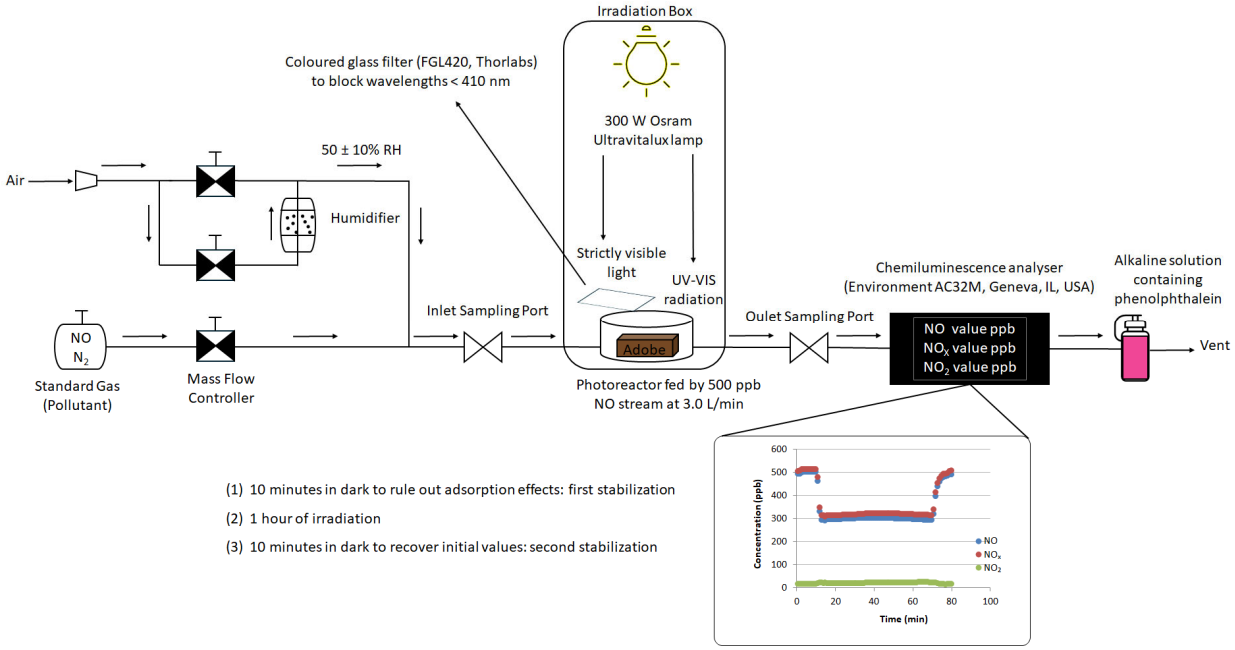

Figure 4. Schematic representation of the experimental setup used for the photocatalytic activity evaluation (NO_X removal test).

2.2.6. Life Cycle Assessment (LCA) and Life Cycle Costing (LCC)

(a) Methodological framework

The environmental and economic assessment was conducted following ISO 14044: 2006 [62], and ISO 15686-5:2017 [63]. The Life Cycle Assessment (LCA) methodology defined in ISO 14044 comprises four main phases: (1) goal and scope definition, (2) life cycle inventory analysis, (3) life cycle impact assessment, and (4) interpretation.

Due to the high variability among buildings and the large number of parameters influencing construction costs, a case-study approach was adopted. The reference building

is a single-story social dwelling with a usable floor area of 40.3 m^2, consisting of a kitchen, living room, bedroom, and bathroom, and designed for a service life of 50 years. Detailed information on this baseline building has been previously reported [64]. Its structural model consists of cast-in-place reinforced concrete walls with metal formwork (RCW model).

The functional unit (FU) was defined as 1 m^2 of total built-up area.

The objective of this study is to evaluate the environmental and economic implications of replacing reinforced concrete walls with adobe masonry. The adobe bricks were assumed to be treated with the developed multifunctional coatings to improve durability during the estimated 50-year service life. According to the manufacturer's recommendations, the coatings were assumed to be renewed every 10 years to maintain protection against moisture, rain, water damage, and stains.

Because the use of adobe in structural elements may compromise load-bearing capacity, cement-based materials were retained for foundations, floor slabs, beams, and columns.

Four life-cycle stages were considered:

- Manufacturing.
- Construction.
- Use.
- End-of-life.

In parallel with the LCA, a Life Cycle Costing (LCC) analysis was performed following ISO 15686-5:2017 [63], excluding externalities and financial costs.

(b) Manufacturing stage

The manufacturing stage includes raw material extraction, processing, manufacturing, energy consumption, and associated emissions. The materials considered in the analysis were clay roof tiles, concrete, cement, glass, aluminum, wood, adobe, $LaFeO_3$ nanoparticles, and hydrophobic and hydro-oleophobic agents (W and O).

- Construction materials

The production of roof tiles involves clay extraction and preparation, manual mixing with water, molding, air drying, and kiln firing until final hardening is achieved.

Window manufacturing requires both glass and aluminum components. For glass production, a mixture of silica, sodium carbonate, and limestone is melted at approximately 1500 °C and formed using the float process, in which the molten mixture is poured onto molten tin followed by controlled cooling (annealing). The glass is then cut to the required dimensions.

Aluminum frames are produced through extrusion, followed by cutting, machining, corner assembly, and installation.

The fabrication of doors and frames relies on wood processing, including timber selection and drying, machining of grooves and joints, preparation of openings for hinges and locks, component assembly, and finishing operations such as sanding, varnishing, or painting.

Cement production involves the extraction of limestone, clay, and gypsum, followed by crushing, mixing, kiln calcination at approximately 1500 °C to produce clinker, and subsequent grinding.

Concrete production requires mixing cement, water, aggregates, and additives, followed by pouring into molds or formwork, compaction, and curing.

- Adobe production

Adobe production was assumed to occur in situ, using soil extracted during excavation works. The process includes mixing soil with water, molding blocks of 40 × 20 × 30 cm (30 cm thickness), and air-drying. Approximately 13 adobe blocks are required per m^2 of wall surface. The total required number of adobe blocks was calculated as follows:

Total wall area: 33.48 m (total length of the walls, internal and external) × 2.80 m (wall height) = 93.744 m^2.

Brick face area: 0.40 m × 0.20 m = 0.08 m^2. However, in adobe construction, a bonding joint (mud mortar) of approximately 1.5 cm is typically left both horizontally and vertically. This increases the effective area covered by each brick. Effective length: 0.40 + 0.015 = 0.415 m. Effective height: 0.20 + 0.015 = 0.215 m. Effective area per brick: 0.415 × 0.215 = 0.089225 m^2.

Thus, the number of real adobe bricks required is the total wall area divided by the adjusted surface area occupied by each adobe brick, including the correction for the mortar joints used to bond the bricks together: 93.744 m^2/0.089225 m^2 = 1051 units.

Finally, considering that adobe is a relatively fragile material, and some units commonly break during preparation or placement, a waste factor (5–10%) should be assumed. With a 7% allowance, that would imply 1051 × 1.07 = 1125 adobe bricks.

- Protective coatings and nanoparticles

Due to industrial confidentiality, the environmental and economic assumptions for the protective media and nanoparticles were based on commercial labels, literature data, and market information.

$LaFeO_3$ nanoparticles were assumed to be synthesized by Flame Spray Pyrolysis (FSP), as described in the Materials and Methods section. In this simplified model, a mixture of metal nitrates and isopropanol is atomized into a flame fueled with O_2 and N_2. Combustion produces CO_2 and H_2O, while the resulting powder primarily consists of $LaFeO_3$, with possible traces of nitrogen oxides, carbonates, and lanthanum or iron oxides.

Considering that lanthanum strontium cobalt ferrite (LSCF) costs 566 $/150 g [65], the price of $LaFeO_3$ was estimated at 180 $/150 g, reflecting the absence of cobalt and strontium. Assuming an exchange rate of 1 $ = 0.85 €, this corresponds to 153 €/150 g.

Production impacts were estimated using data from similar metal oxide nanoparticles. It was assumed that producing 1 kg of $LaFeO_3$ requires 200 MJ of energy and generates 10 kg of CO_2 [66,67].

The commercial coatings Tecnadis PRS Performance (O-type) and Tecnadis Aquashield Forte (W-type) were assumed to contain 85% isopropanol and 15% ceramic nanoparticles, resulting in embodied energy values of approximately 52 MJ/kg and emissions of 2.3 kg CO_2/kg [68,69].

Based on product densities, impacts per liter were calculated as:

- O-type: 40.9 MJ and 1.85 kg CO_2.
- W-type: 41 MJ and 1.80 kg CO_2.

Estimated prices were 19.40 €/L (O-type) and 14 €/L (W-type).

According to the manufacturer, coating coverage ranges between:

- 4–12.5 m^2/L for O-type.
- 4–9 m^2/L for W-type.

Average values of 8 m^2/L and 6.5 m^2/L were adopted. Each application requires two passes, and coatings must be renewed every 10 years. To cover 1 m^2, material sufficient for 10 m^2 must be purchased, corresponding to 2 L of each medium. Surplus material was not considered waste because it can be stored and used in future projects.

For the LCA and LCC analyses, the nanoparticle concentration was assumed to be 5% (g nanoparticles per mL carrier medium). Using 2 L of suspension per medium, 100 g of nanoparticles were required for each formulation.

To minimize environmental and economic impacts, the coatings were assumed to be prepared on site by manual mixing.

However, it should be noted that certain approximations were made regarding the coating components (dispersant medium and nanoparticles), as the exact formulations are subject to industrial confidentiality. Given the high volume of the dispersant relative to the additive materials, any potential deviations resulting from these approximations are expected to be non-significant and unlikely to affect the overall conclusions.

(c) Cement reduction through adobe substitution

For the adobe-based house, cement, concrete, roof tiles, door and window components, nanoparticles, and coating media were assumed to be manufactured in factories, and therefore their production impacts, purchase costs, and transportation emissions were included.

Using 1 m^2 as the functional unit, the required material quantities were derived from the control building data.

An estimation of the reduction in cement content was performed using the linear dimensions reported for the reference building [64]: 21.68 m of exterior walls and 11.8 m of interior walls, giving a total wall length of 33.48 m. For consistency with the reference model, a thickness of 0.10 m was assumed for the foundation/floor slab, walls, and beams.

The calculated concrete volumes were:

- Foundation/floor slab: 40.3 m^2 × 0.10 m = 4.03 m^3.
- Walls (2.80 m height): 33.48 m × 2.80 m × 0.10 m = 9.37 m^3.
- Tie beams: 33.48 m × 0.10 m × 0.10 m = 0.33 m^3.

Thus, the total concrete volume of the control building was 13.73 m^3.

When replacing concrete walls with adobe, an important structural constraint arises: adobe walls cannot be built with a thickness of 10 cm because such dimensions would be structurally unstable. For adequate stability, adobe walls require a minimum thickness of approximately 30 cm. This requirement implies widening the bond beam and the bearing zone on the slab, even if the slab thickness remains 10 cm. Concrete bond beams above adobe walls are required for structural bracing and confinement, particularly in seismic regions, and therefore this portion of cement consumption cannot be eliminated.

The revised concrete requirements were:

- Foundation/floor slab: unchanged, 4.03 m^3.
- Bearing reinforcement strip: 33.48 m × 0.30 m × 0.10 m = 1.00 m^3.
- Adobe walls: concrete eliminated (9.37 m^3 reduction).
- Bond beams: 33.48 m × 0.30 m × 0.15 m = 1.51 m^3.

The total concrete volume in the adobe scenario was 6.54 m^3, corresponding to a cement reduction of 52.37%.

Although the concrete wall volume is eliminated, the wider bond beams required for adobe walls partially offset the potential savings. Nevertheless, the reduction is consistent with values reported in previous studies [70].

(d) Construction stage

The construction stage includes material assembly and in situ construction activities, considering machinery use, labor, energy consumption, and waste generation. For the control building, energy demands were estimated as follows [64]:

- Preliminary works: 117.43 MJ.
- Cast-in-place concrete walls: 40.51 MJ.
- Floor slab: 11.69 MJ.
- Masonry works: 0.06 MJ.

CO_2 emissions were estimated using an emission factor of 0.08 kg CO_2/MJ, assuming electricity as the main energy source [71]. In the adobe house scenario, reinforced concrete walls were replaced with adobe walls, reducing the associated construction energy to 8 MJ,

reflecting the lower energy intensity of adobe construction. Based on literature values, a 30% reduction in construction effort was assumed [70].

(e) Use and maintenance stage

The use stage considers preventive maintenance activities required to ensure a 50-year service life. Protective coatings applied to adobe walls were assumed to be renewed every 10 years, resulting in five applications during the building lifetime. Each renewal involves transport and application activities requiring 255.40 MJ, assuming a 30 km round trip and one full working day.

In the control building, no nanoparticles or hydrophobic/oleophobic coatings are applied. Instead, an anti-carbonation protective paint (2.24 kg) is used, also renewed every 10 years.

(f) End-of-life stage

At the end-of-life stage, the building is demolished. Demolition of reinforced concrete structures typically involves intensive machinery use, labor, and waste management.

Replacing reinforced concrete walls with adobe was assumed to reduce demolition time by approximately one-third compared with conventional reinforced concrete demolition [72].

(g) Transportation, machinery, and labor assumptions

All materials except adobe bricks were assumed to be produced in factories located 30 km from the construction site, requiring a round trip for transport. Non-reusable waste was assumed to be transported to a landfill located 7 km away.

A 10,000 kg capacity truck with 15 m^3 container volume operating with Euro 6 diesel fuel was assumed. Fuel consumption was 35 L/100 km, with diesel priced at 1.50 €/L, generating 2.68 kg CO_2/L and 1.15 kg water consumption/L [73,74].

Excavation and demolition were assumed to be carried out using an excavator consuming 20 L/h of diesel. Labor costs were based on a crew of five workers, each earning 1200 € per month for a 40 h workweek (7.5 €/h).

Construction tasks were assumed to require:

- 1 week for mixing and preparation of materials.
- 4 h for excavation.
- 2 weeks for demolition and debris removal.
- 24 weeks for construction of the house.

(h) Comparative evaluation

To determine whether adobe bricks produced in situ from excavated soil provide improvements in terms of cost, energy consumption, and CO_2 emissions, the LCA and LCC results of the adobe-based house were compared with those of the control case building.

The values reported in Table 2 were derived from previously available data and complemented with justified assumptions to address missing information [75–77].

Table 2. Price, CO_2 emissions, and embodied energy of materials used in the control case building.

Material	Price	CO_2	Energy
Concrete 20 MPa	90 €/m^3	242 kg CO_2/m^3	1840 MJ/m^3
Reinforcing steel	2.2 €/kg	1.9 kg CO_2/kg	22.5 MJ/kg
Concrete brick	0.33 €/kg	0.25 kg CO_2/kg	2.25 MJ/kg
Cement mortar	0.15 €/kg	0.23 kg CO_2/kg	2.5 MJ/kg
Brick veneer roof	1.4 €/kg	0.35 kg CO_2/kg	5.0 MJ/kg
Ceramic tile	1.2 €/kg	0.4 kg CO_2/kg	4 MJ/kg
Lime mortar	0.30 €/kg	0.18 kg CO_2/kg	1.5 MJ/kg

Table 2. *Cont.*

Material	Price	CO_2	Energy
Latex paint	5 €/kg	2.5 kg CO_2/kg	17.5 MJ/kg
Aluminium window/door frame	5 €/kg	9.0 kg CO_2/kg	170 MJ/kg
Glass	2.5 €/kg	0.85 kg CO_2/kg	20 MJ/kg
Wood door frame	70 €/m^2	1.1 kg CO_2/m^2	56 MJ/m^2
Water (excluding concrete mix)	0.0004 €/kg	0.00003 kg CO_2/kg	0.0004 MJ/kg
Primers, resins and release agents	9 €/kg	5 kg CO_2/kg	65 MJ/kg

Figure 5 illustrates the overall experimental workflow, from the synthesis and characterization of the photocatalytic nanoparticles to their dispersion, application onto the substrates, and subsequent performance evaluation.

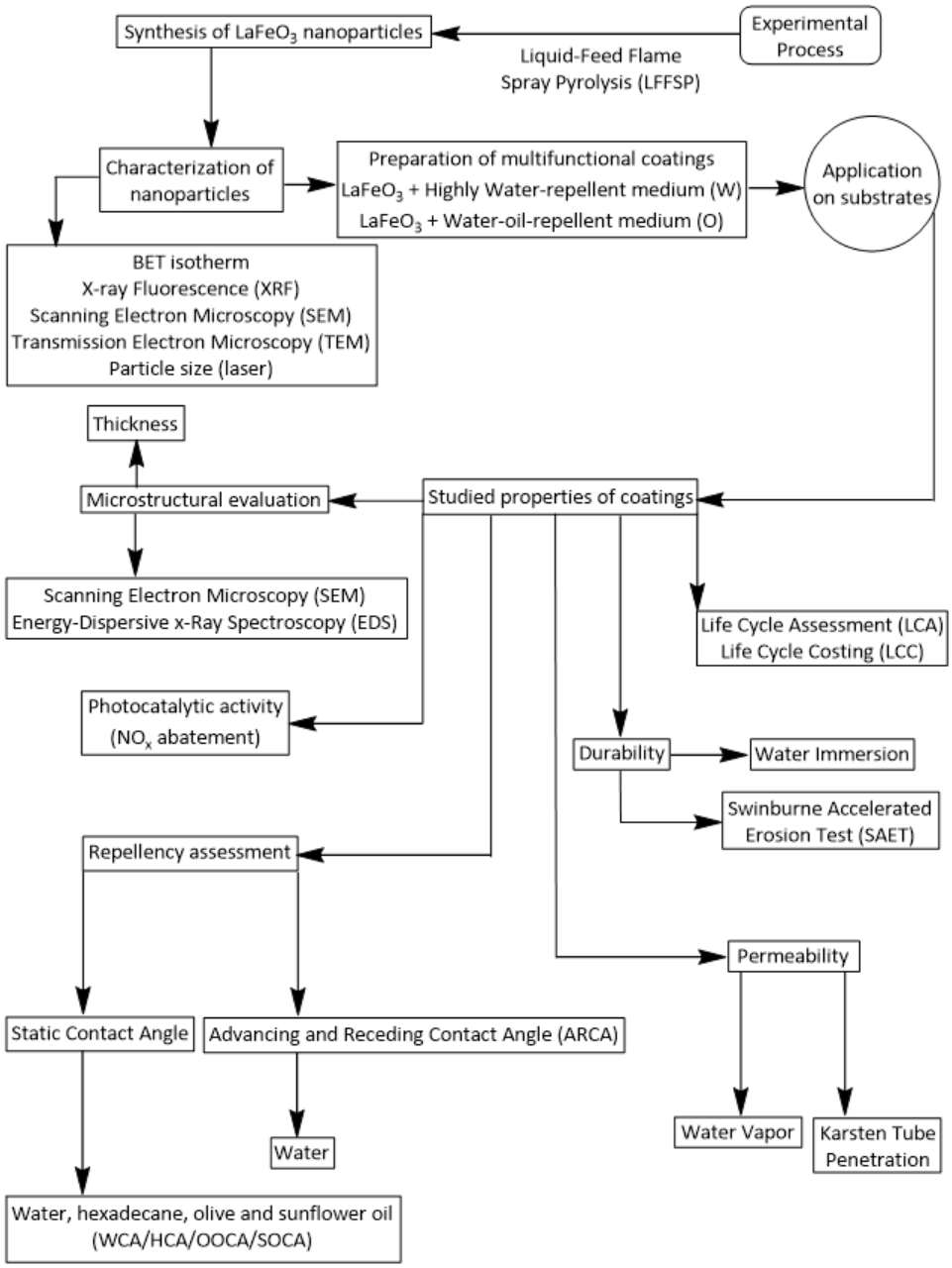

Figure 5. Schematic representation of the experimental process.

3. Results and Discussion

3.1. Characterization of Raw Materials

3.1.1. $LaFeO_3$ Nanoparticles and Dispersing Media

The chemical composition of the nanoparticles, determined by X-ray fluorescence (XRF) analysis, revealed that $LaFeO_3$ nanoparticles consisted predominantly of Fe and La, with an elemental ratio expressed as oxides (Fe_2O_3/La_2O_3) of 1.17. The X-ray diffraction (XRD) pattern, shown in Figure 6, indicated the presence of lanthanum orthoferrite (ICDD 37-1493), exhibiting an orthorhombic perovskite structure ($LaFeO_3$). Rare-earth orthoferrites ($REFeO_3$) adopt a crystal structure in which a central iron ion coordinated by six O^{2-} anions, forming an octahedral FeO_6 arrangement. The rare-earth cations (R) are coordinated with twelve O^{2-} anions located between the FeO_2 structural units [78]. No additional crystalline phases were detected, suggesting that the synthesis procedure successfully promoted the formation of phase-pure lanthanum orthoferrite.

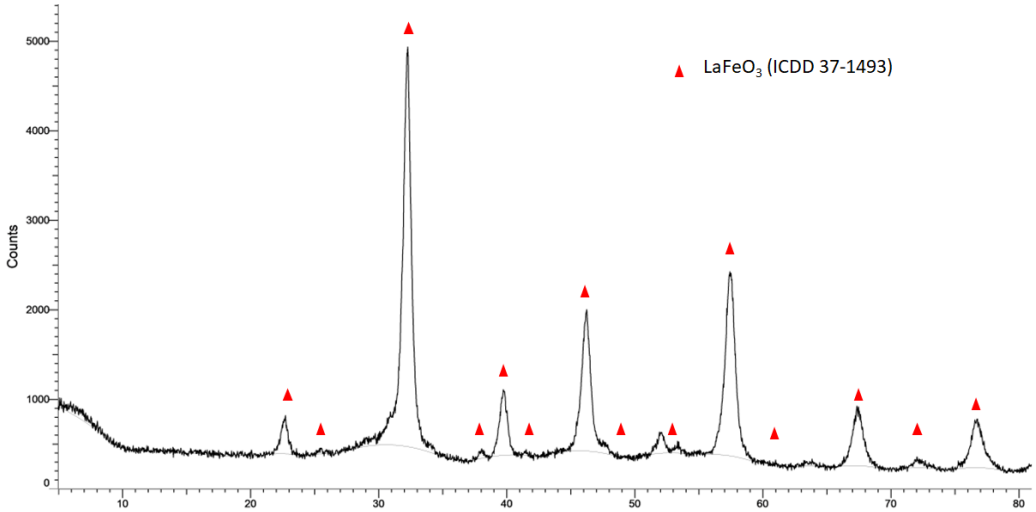

Figure 6. X-ray diffraction patterns of $LaFeO_3$ nanoparticles.

The specific surface area, determined by N_2 adsorption using the Brunauer–Emmett–Teller (BET) method, was 46.25 $m^2\ g^{-1}$, which falls between the values reported for other nanostructured photocatalysts, such us Nano-Zn_2TiO_4-ZnO (69.4 $m^2\ g^{-1}$) [39] and Nano-$Bi_{12}ZnO_{20}$-ZnO (30.6 $m^2\ g^{-1}$) [43].

Figure 7a,b show TEM images of the synthesized nano-heterostructure, revealing well-defined morphology and nanoscale features. The images confirm the formation of structured nanoparticles with a clear tendency to agglomerate. Figure 7c,d present SEM micrographs of $LaFeO_3$ nanoparticles, showing agglomerated structures with a loosely packed arrangement.

Figure A1 (Appendix A) presents the particle-size distributions obtained from suspensions with different $LaFeO_3$ contents. The carrier media W and O already contain ceramic nano-oxides, which explains the particle-size distributions observed in the base formulations. The W medium exhibits a relatively narrow distribution centered at approximately 0.7 µm, whereas the O medium shows larger particles with a characteristic size around 50 µm. Upon incorporation of $LaFeO_3$, the distributions shift toward larger mean particle sizes (approximately 100 µm) and become noticeably broader, indicating increased polydispersity and the formation of larger aggregates. The absence of peaks in the sub-micrometric region supports the hypothesis that the nanoparticles are present predominantly as agglomerates rather than isolated primary particles.

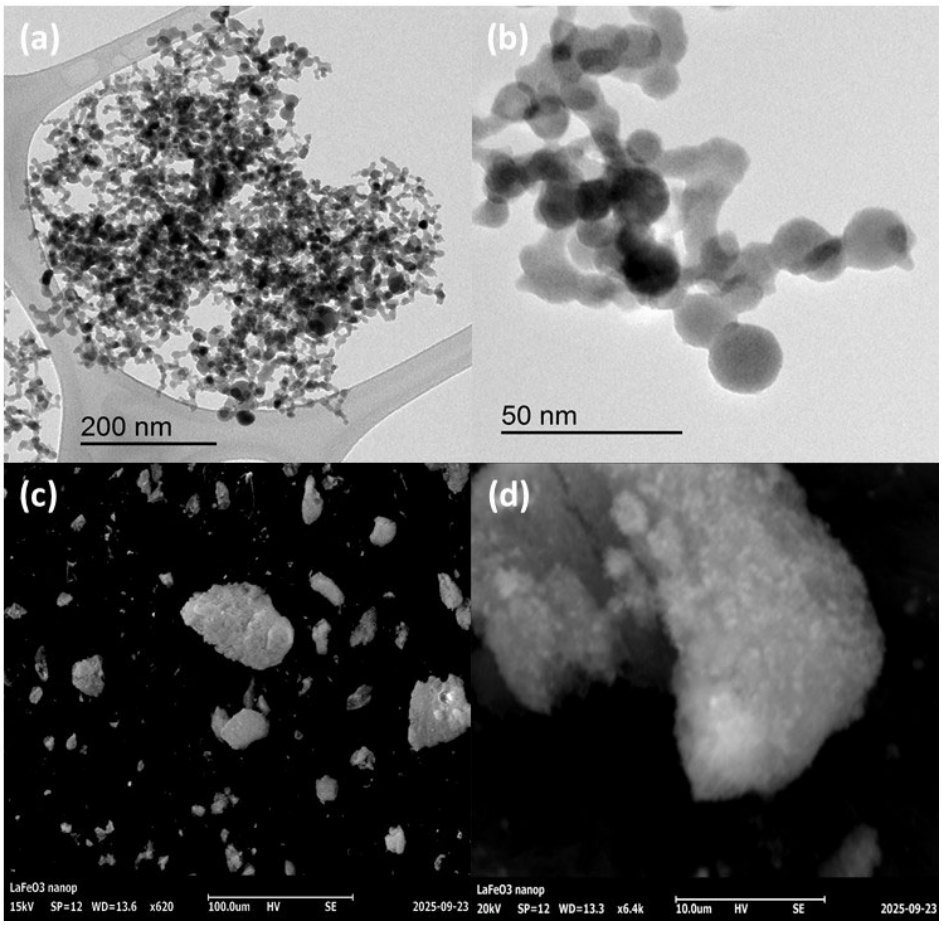

Figure 7. (**a**,**b**) TEM images of $LaFeO_3$ nano-heterostructure showing particle morphology at different magnifications. SEM micrographs of $LaFeO_3$ nanoparticles at (**c**) 620 and (**d**) 6400 magnifications.

Figure 8 illustrates the photocatalytic performance of the pure nanoparticles, evaluated by monitoring their NOx removal efficiency under both solar and visible light irradiation. Under solar irradiation, $LaFeO_3$ nanoparticles achieved NO_x removal rates of up to 20%, whereas in the absence of UV radiation the efficiency decreased to 6%.

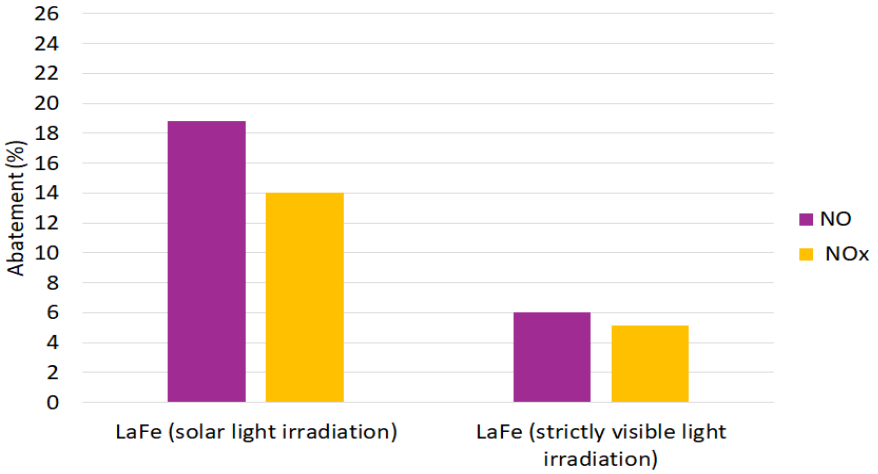

Figure 8. NO and NO_x removal efficiencies of $LaFeO_3$ nanoparticles under solar and visible light irradiation.

Although catalysts with higher photocatalytic activity have been reported, such as titanium-zinc oxides or bismuth-zinc oxides [43], the darker coloration of $LaFeO_3$ makes it

more suitable for applications where preservation of the natural appearance of substrates such as adobe is required. Importantly, $LaFeO_3$ effectively reduced NO concentration without generating significant amounts of NO_2. The selectivity, defined as the ration between the NO_x removal rate and the NO removal rate (S = NO_x removal rate/NO removal rate), was 74.8% under solar irradiation, and 85.5% under strictly visible light. These values indicate that $LaFeO_3$ nanoparticles predominantly convert NO into non-toxic nitrates, rather than releasing the undesirable intermediate NO_2. As previously reported [79,80], $LaFeO_3$ can adsorb both NO and NO_2, mainly through interactions with iron active sites, while the presence of oxygen vacancies further enhances adsorption capacity. Consequently, the catalyst promotes NO_2 adsorption followed by its oxidation to nitrate species.

3.1.2. Adobes

The mineralogical composition of the raw earth used for adobe production was determined by X-ray diffraction (XRD) analysis. The diffraction pattern shown in Figure 9 exhibits basal reflections at several 2θ values. The peaks observed at 10.04 Å, 4.98 Å, and 3.34 Å correspond to illite, while the reflections at 7.13 Å and 3.57 Å are attributed to kaolinite [81–83]. These peaks remain essentially unchanged after ethylene glycol treatment and heating at 500 °C, indicating the absence of expandable clay minerals, such as smectites. Overall, the results suggest that the raw earth used for the adobe specimens is predominantly composed of illite and kaolinite.

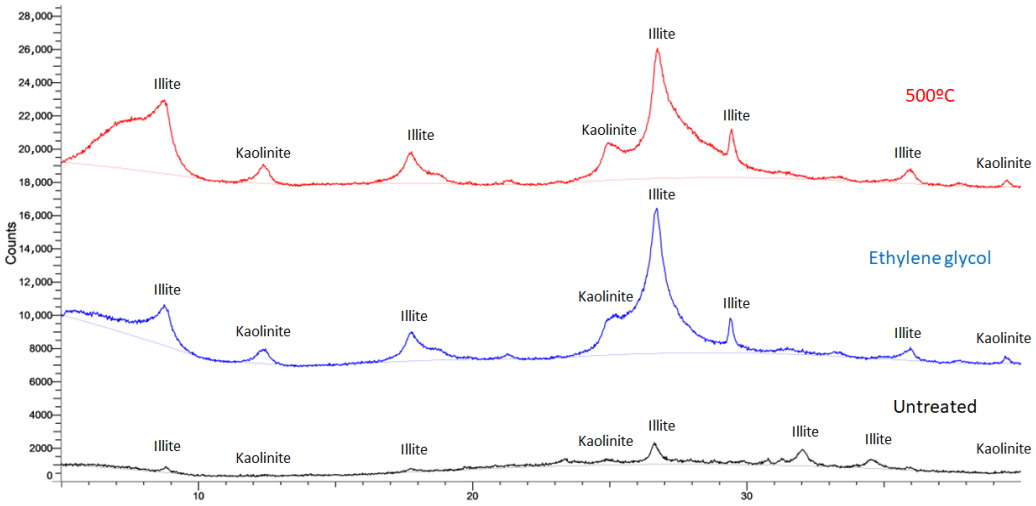

Figure 9. X-ray diffraction (XRD) pattern of adobe raw material.

Figure 10 shows the SEM and EDS results obtained for the adobe samples. The surface exhibits a highly heterogeneous morphology, which is typical of unstabilized adobe materials. The elemental composition highlights the presence of silicon, aluminum, and oxygen, consistent with the X-ray diffraction results indicating that the material is predominantly composed of illite and kaolinite. Although the EDS analysis shows only a minor presence of potassium, this element is commonly associated with illite minerals. The limited presence and irregular distribution of iron and magnesium suggest the occurrence of minor oxides or accessory minerals. Additionally, the dispersed presence of calcium may indicate traces of soluble salts incorporated in the original clay, very fine carbonate particles, fine soil fractions, or the partial weathering of feldspars.

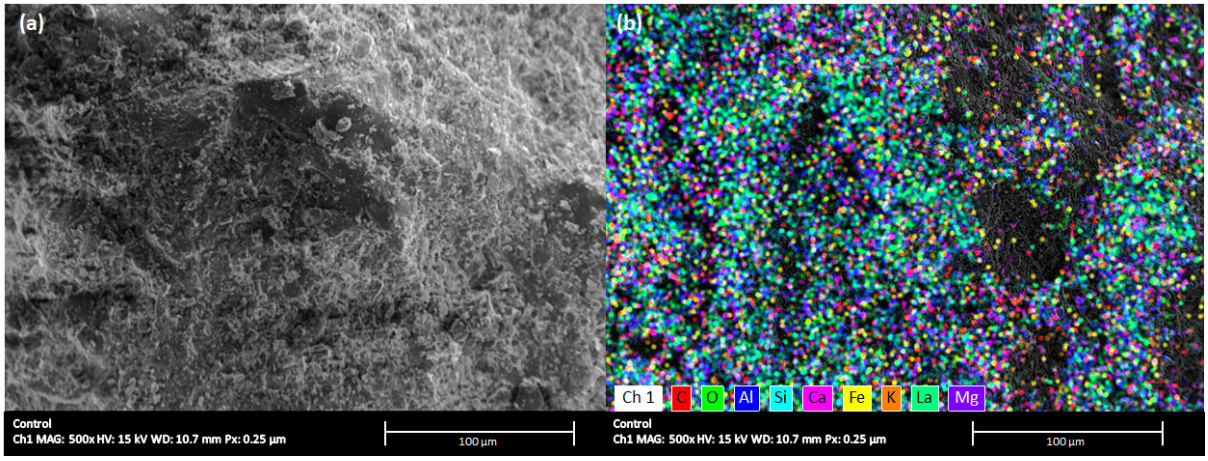

Figure 10. Microstructural features of the adobe sample: (**a**) SEM micrograph and (**b**) EDS multi-element mapping.

3.2. Microstructural Assessment of the Coatings

Figures 11 and 12 present representative SEM images of the coatings applied onto adobe substrates. The micrographs reveal structures with varied shapes and sizes, predominantly spherical particles, as well as the presence of cracks and pores. The coatings appear non-uniform, which is likely related to the inherent surface irregularity of the adobe substrate.

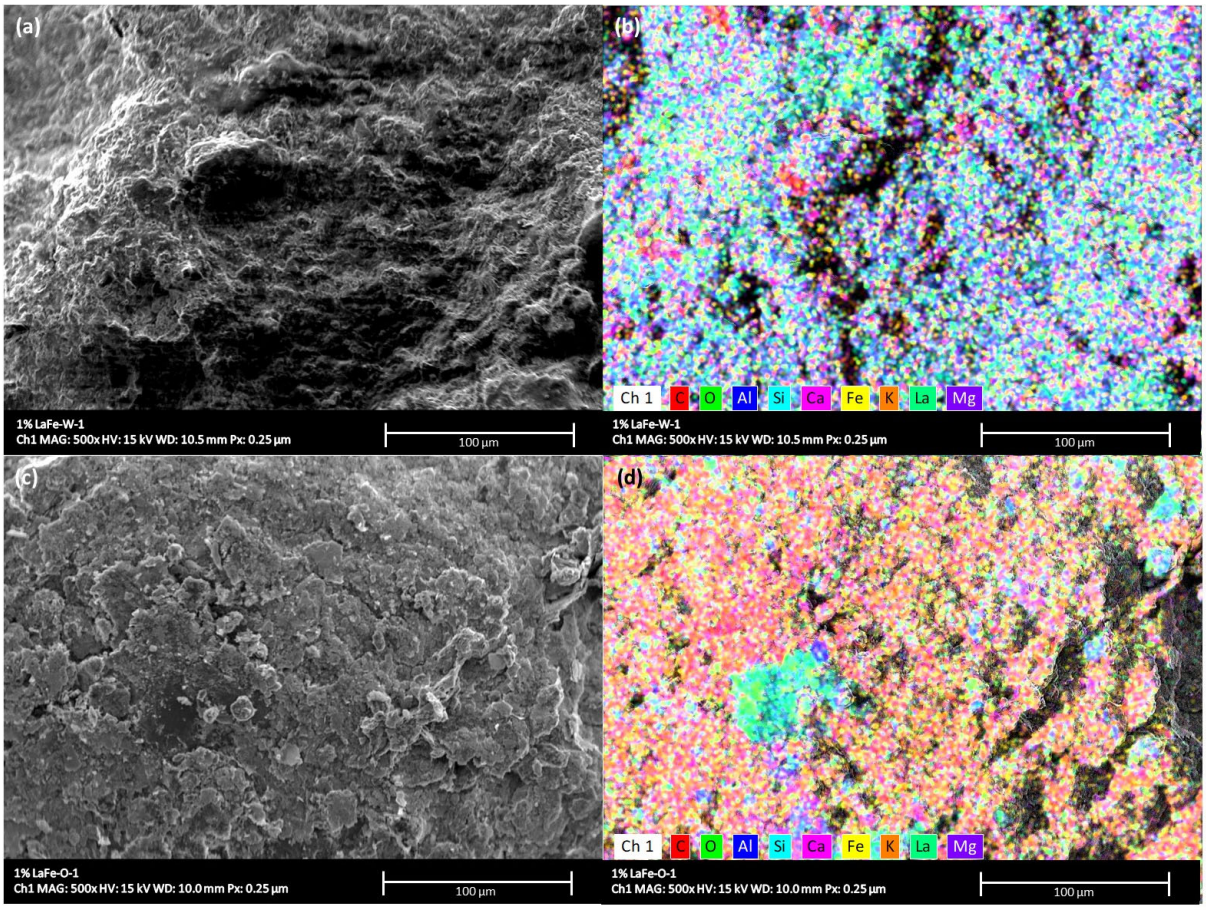

Figure 11. SEM analysis of adobe coatings with LaFe. SEM micrographs of coatings prepared with the highly water-repellent medium (W): (**a**) 1% LaFe-W-1; corresponding EDS multi-element mapping (**b**); coating with the water-oil-repellent medium (O): (**c**) 1% LaFe-O-1; corresponding EDS multi-element mapping (**d**).

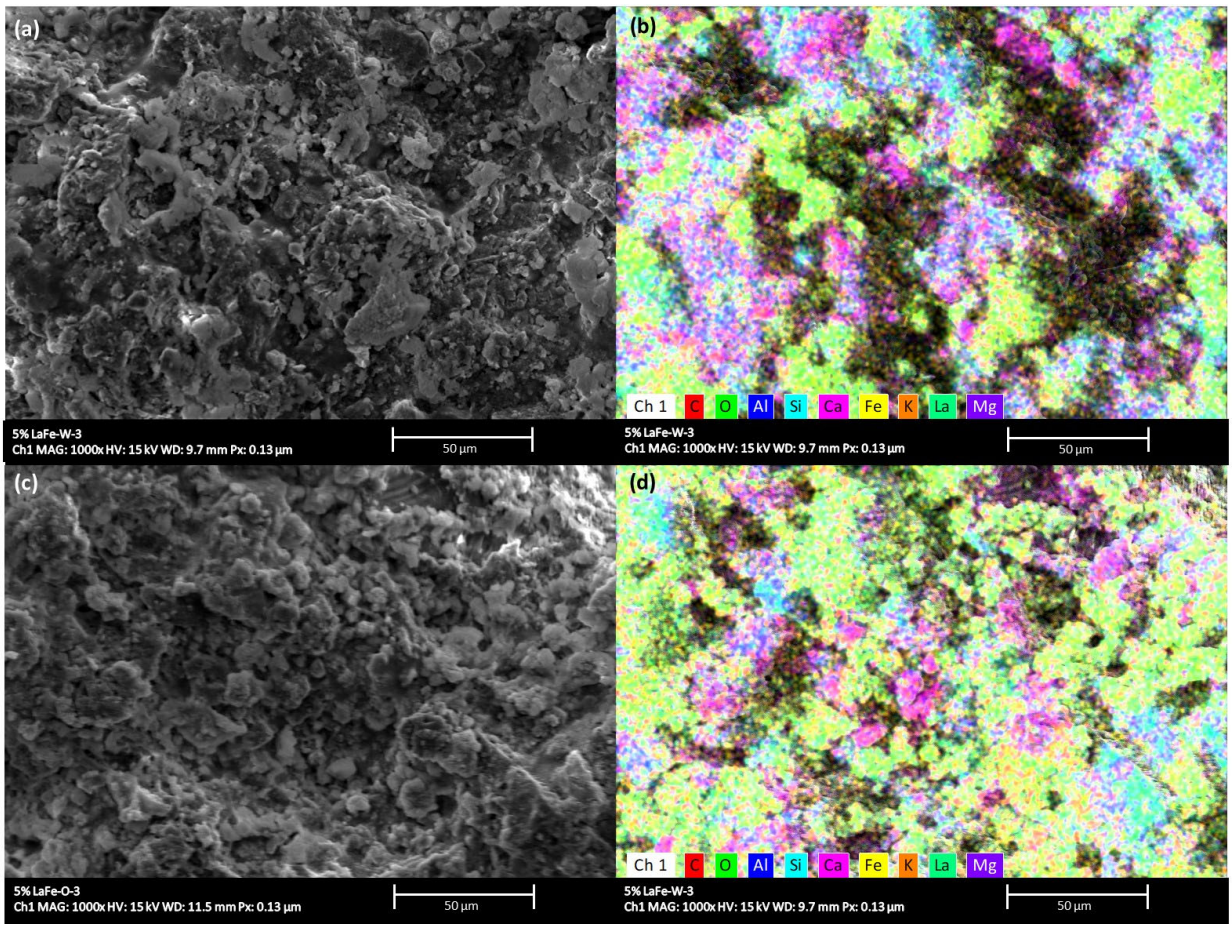

Figure 12. SEM analysis of adobe coatings with LaFe. SEM micrographs of coatings prepared with the highly water-repellent medium (W): (**a**) 5% LaFe-W-3, corresponding EDS multi-element mapping (**b**); coating with the water-oil-repellent medium (O) (**c**) 5% LaFe-O-3, corresponding EDS multi-element mapping (**d**).

A comparison between the 1% LaFe-W-1 and 1% LaFe-O-1 formulations (Figure 11) and the 5% LaFe-W-3 and 5% LaFe-O-3 formulations (Figure 12) show a significantly higher presence of iron and lanthanum in the latter samples. This result is expected, as the catalyst loading was increased fivefold and three consecutive coating applications were performed in these formulations. Consistently, Figures A2–A6 (Appendix A) show a progressive increase in the distribution of lanthanum and iron, ranging from minimal levels in the control sample, to moderate levels in the 1% LaFe-W-1 and 1% LaFe-O-1 samples, and high concentrations in the 5% LaFe-W-3 and 5% LaFe-O-3 samples. In the latter cases, lanthanum- and iron-rich agglomerates can be clearly observed, in agreement with the agglomeration behavior previously identified in Figure 7.

The study of multifunctional coatings for the protection of raw earth substrates is relatively recent, so further experimental research is required to optimize variables such as agglomeration. Potential strategies to reduce agglomeration involve modifications to the protocol: prolonged or high-energy sonication [84], the use of dispersing agents compatible with the coating [39,43], optimization of drying [85], or alterations to the carrier medium to improve nanoparticle stabilization [86].

Coatings prepared with the W medium appear more homogeneous than those prepared with the O medium, providing more uniform coverage of the substrate. This behavior has also been reported in previous studies [43]. Furthermore, Figure A1 (Appendix A) shows that the particle size in suspensions prepared with the W medium is generally

smaller than those prepared with the O medium, which may facilitate a more uniform distribution and improved homogenization of the coatings.

Figure 13 presents the thickness values measured for different coatings. The results range from 32.5 to 52.0 µm. The control sample (C) shows the lowest thickness (32.5 µm), whereas the 3% LaFe-O-2 and 5% LaFe-O-2 samples exhibit the highest values (52.0 µm). A comparison between the control sample and the W-1, W-2, W-3, O-1, O-2, and O-3 samples indicates that the application of the repellent media slightly increased the coating thickness to 35.0–36.5 µm, particularly in the case of the hydro-oleo-repellent medium. It should be noted that both media contain ceramic nano-oxides and stabilizers, and that the particle size is larger in the hydro-oleophobic medium, as shown in Figure A1 (Appendix A).

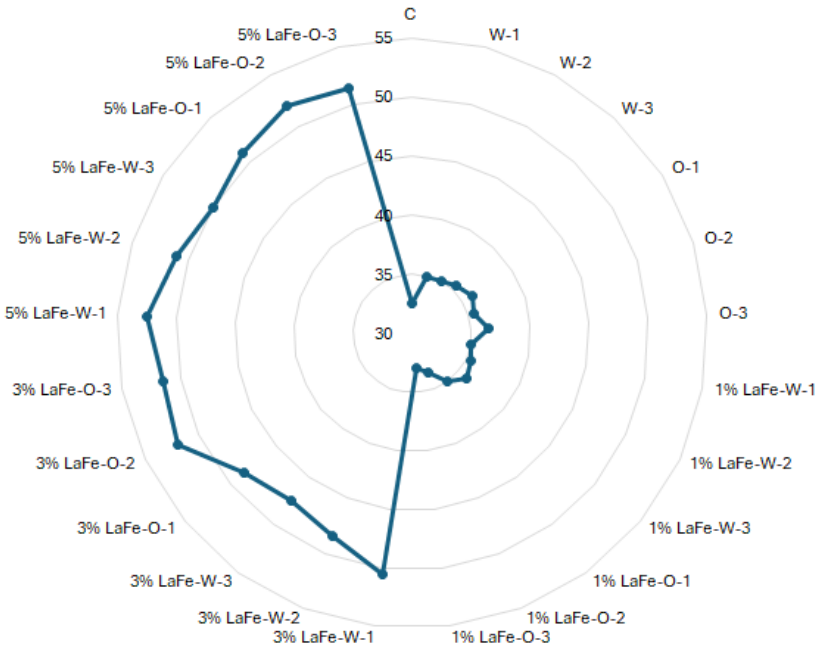

Figure 13. Coating thickness (µm) measured for the nanoparticle-based coatings applied to adobe substrates.

The incorporation of the photocatalyst did not produce significant changes in coating thickness at a 1% loading, with values remaining within the 33.0–36.0 µm range. However, samples containing 3% and 5% $LaFeO_3$ reached thickness values of approximately 47.5–52.0 µm. This increase can be attributed to the agglomeration tendency of the nanoparticles, previously observed in Figure 7. In this regard, Figure A1 (Appendix A) confirms that suspensions containing 3% and 5% photocatalyst exhibited the largest particle sizes.

3.3. Static and Dynamic Contact Angle of the Coatings

Figure 14 presents the static contact angle measurements on the adobe samples. The control sample exhibited a strong affinity for all four tested liquids, which were rapidly absorbed into the substrate, preventing reliable contact angle measurements. The applied coatings proved effective in improving liquid repellency. For water droplets, the measured contact angles exceed 90° for both carrier media (W and O), indicating that the coatings successfully imparted hydrophobic properties to the adobe substrates. The treated surfaces also displayed low surface energies, which hindered liquid-surface interactions. Several samples approached the superhydrophobicity threshold (150°), with particularly notable values for 3% LaFe-W-2 (136.2°), 5% LaFe-W-1 (136.2°), 3% LaFe-O-2 (132.6°), and 5% LaFe-O-3 (132.6°).

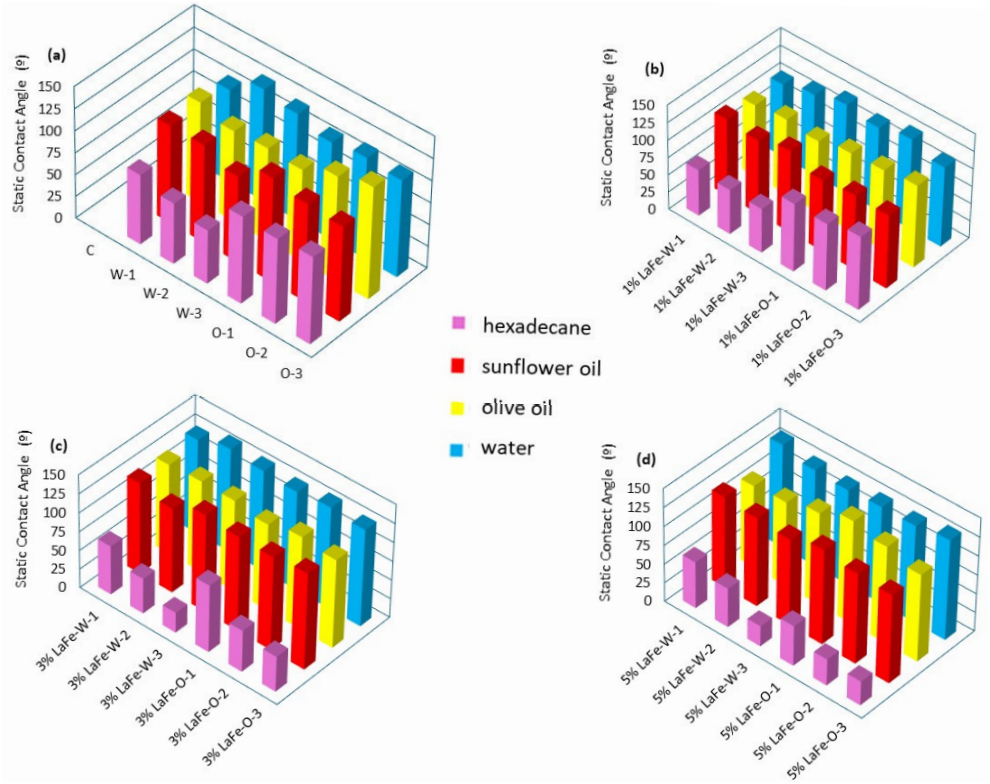

Figure 14. Static contact angle measurements for (**a**) control samples, (**b**) 1% LaFe, (**c**) 3% LaFe, and (**d**) 5% LaFe coatings. Contact angles were determined using hexadecane, sunflower oil, olive oil, and water. All samples include coating prepared with W (highly water-repellent) and O (water- and oil-repellent) media.

Regarding oil repellency, the contact angles measured with olive and sunflower oils were slightly lower than those obtained with water, although they remained within a comparable range. Importantly, none of the values fell below oleophobicity threshold (90°). Some samples even approached the superoleophobicity limit (150°), such as 5% LaFe-O-1, which reached 135.4° in olive oil.

Given the promising results obtained for olive and sunflower oils, additional measurements were performed using a more non-polar liquid, hexadecane. After changing the solvent, the repellency performance decreased comparatively, and most coatings did not reach the oleophobicity threshold (90°), except for the following: 1% LaFe-O-1 (97.5°), 1% LaFe-O-2 (95.8°), and 1% LaFe-O-3 (104.8°).

Overall, the contact angle values followed the general trend water > natural oils > hexadecane. This behavior can be explained by the surface free energies of the tested liquids: water (72.8 mN/m) [87], olive oil (32.03 mN/m) [88], sunflower oil (33.5–34.0 mN/m) [89], and hexadecane (27.5 mN/m) [87]. A substrate is typically considered liquid-phobic when its surface free energy is at least 25% lower than of the liquid [87]. In this context, cohesive interactions in water are dominated by hydrogen bonding, whereas London dispersion forces govern cohesion in oils and other non-polar liquids. Consequently, more energy is required to disrupt the strong hydrogen-bonding network in water, and this energy is not compensated by the relatively weaker adhesive interactions with the substrate. As a result, water droplets tend to exhibit higher contact angles than other liquids. Previous studies have also reported that coatings prepared with the highly water-repellent formulation (W) exhibit higher water contact angles than those prepared with the water- and oil-repellent formulation (O) [39]. Conversely, this trend is reversed when oil-based liquids are considered.

Figure 15 visually illustrates the comparative behavior of several liquid droplets on the coated adobe surfaces. Figure 15(a_1,a_2) compare the water-repellent performance of the two tested media (W and O), clearly showing that the highly hydrophobic formulation (W) provided greater water repellency than the hydro-oleophobic formulation (O).

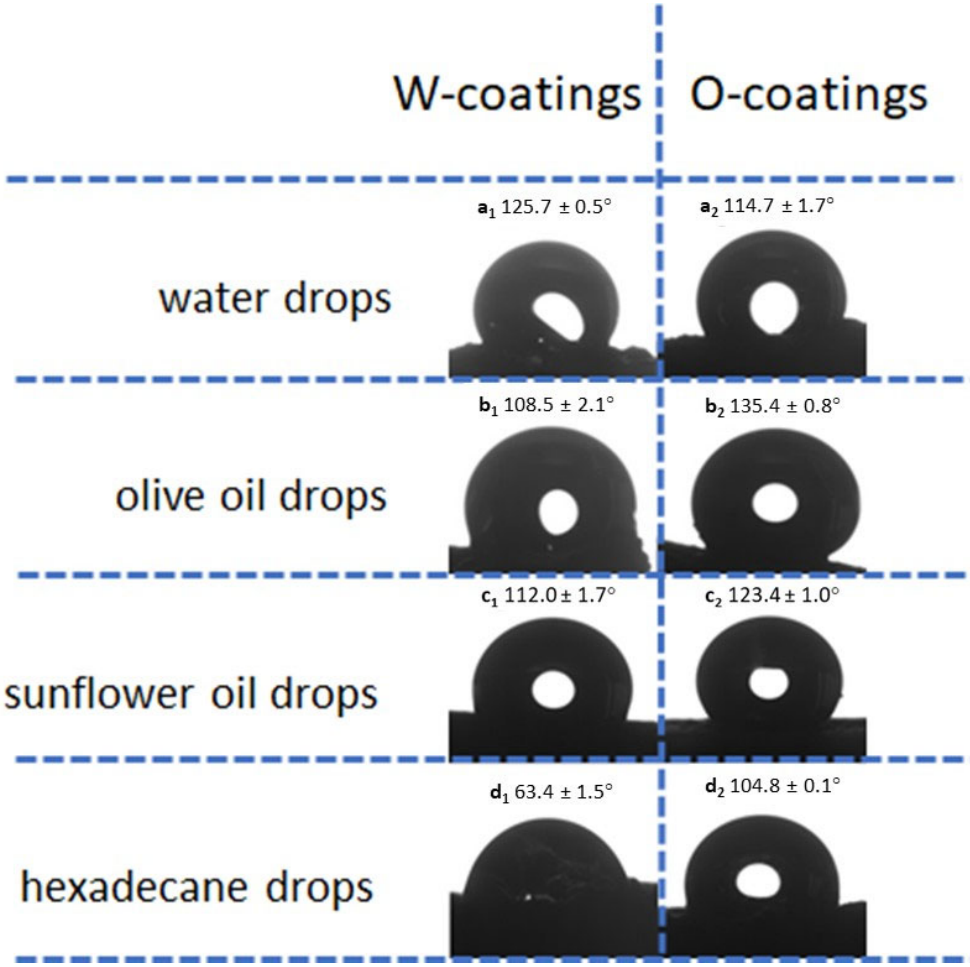

Figure 15. Representative static contact angles for different liquids: water droplets (**a_1**) 1% LaFe-W-3 and (**a_2**) 1% LaFe-O-3; olive oil droplets (**b_1**) 5% LaFe-W-1 and (**b_2**) 5% LaFe-O-1; sunflower oil droplets (**c_1**) 3% LaFe-W-2 and (**c_2**) 3% LaFe-O-2; hexadecane droplets (**d_1**) 1% LaFe-W-3 and (**d_2**) 1% LaFe-O-3.

Figure 15(b_1,b_2) compare the repellency of olive oil for both media, while Figure 15(c_1,c_2) present droplets of sunflower oil, and Figure 15(d_1,d_2) show droplets of hexadecane. In these three cases, the images clearly demonstrate that the hydro-oleophobic medium (O) exhibits a higher oleo repellent capacity than the highly hydrophobic medium (W), as evidenced by the larger contact angles observed for these liquids.

Dynamic water contact angle measurements, or ARCA (Advancing and Receding Contact Angle analysis), were performed to obtain a more comprehensive evaluation of the coated surfaces, which exhibit chemical and topological heterogeneities. The results are presented in Figure 16, while the corresponding hysteresis values are reported in Table 3. Contact angle hysteresis, defined as the difference between the advancing contact angle (ACA) and the receding contact angle (RCA), reflects the interaction between the liquid and the surface during droplet movement. This parameter provides information about the level of repulsion or attraction between the liquid and the surface, which is strongly influenced by the hydrophobic properties of the material [39]. The ACA is associated with the resistance of the surface to droplet spreading, whereas the RCA is more closely

related to adhesion forces, describing the interaction between water and the surface during droplet retraction [39]. The absence of zero hysteresis on any of the tested surfaces indicates that the coatings are not perfectly smooth, uniform, or chemically homogeneous. Higher hysteresis values typically suggest significant surface roughness, heterogeneity, or chemical variability, which hinder droplet mobility.

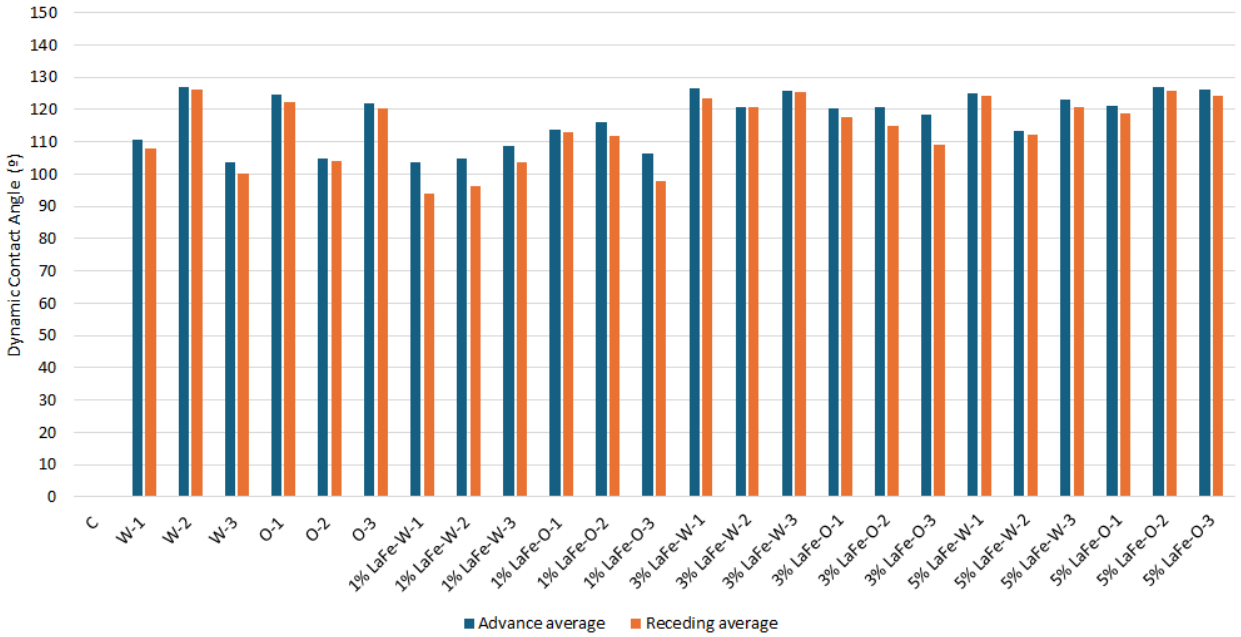

Figure 16. Advancing (ACA) and receding (RCA) water contact angles measured for control and LaFe-coated samples.

Table 3. Contact angle hysteresis values (ACA–RCA) obtained from ARCA measurements using water.

Samples	Hysteresis (Water)	Samples	Hysteresis (Water)
C	-	-	-
W-1	3.58	O-1	6.43
W-2	5.43	O-2	1.54
W-3	2.58	O-3	1.67
1% LaFe-W-1	9.82	1% LaFe-O-1	2.26
1% LaFe-W-2	8.51	1% LaFe-O-2	4.17
1% LaFe-W-3	3.53	1% LaFe-O-3	9.26
3% LaFe-W-1	2.57	3% LaFe-O-1	2.19
3% LaFe-W-2	0.91	3% LaFe-O-2	7.38
3% LaFe-W-3	3.91	3% LaFe-O-3	2.63
5% LaFe-W-1	1.38	5% LaFe-O-1	3.23
5% LaFe-W-2	1.50	5% LaFe-O-2	5.54
5% LaFe-W-3	2.20	5% LaFe-O-3	1.68

Superhydrophobic surfaces are generally defined as those exhibiting contact angles greater than 150° (the superhydrophobicity threshold) together with hysteresis values below 10° [90]. In the present study, low hysteresis values were experimentally observed, with the highest value corresponding to 1% LaFe-W-1 (9.8°). These values were accompanied by relatively high contact angles, with 5% LaFe-O-2 (126.9°) showing particularly notable

performance. The absence of true superhydrophobic behavior can likely be attributed to the inherent porosity of the adobe substrates and the non-uniform coverage of the applied coatings. This limitation may compromise the long-term durability of the materials, as superhydrophobic behavior is not achieved. Nevertheless, it should be noted that other factors—such as capillary water uptake, resistance to erosion, and coating wear resistance—may exert an equal or even greater influence than hydrophobicity itself on the preservation of the structural integrity of adobe materials. It is also important to note that, nevertheless, the coatings clearly imparted significant liquid-repellent properties to the treated surfaces.

3.4. Influence of the Sealing Action: Water Vapor Permeability and Karsten Tube Penetration Test

An ideal coating should reduce the penetration of liquids of interest (water, olive oil, and sunflower oil), thereby preventing material deterioration. At the same time, it should allow the substrate (adobe) to remain breathable in order to avoid unwanted condensation and the subsequent development of microorganisms (e.g., mold). For this reason, sufficient water vapor permeability must be maintained. Although there are no universally accepted reference values for water vapor permeability, indicative ranges can be established based on previous studies and experimental observations:

(1) According to data from Building Science [91], materials can be classified according to their permeability expressed in perms: $W_p \leq 0.1$ perms (vapor-impermeable), 0.1–1.0 perms (semi-impermeable), 1.0–10 perms (semi-permeable), and Wp > 10 perms (vapor-permeable). One perm (USA) is approximately equivalent to 57.2×10^{-10} kg/m^2·s·Pa.

(2) The work of Narloch et al. (2021) [92], reports several values of the vapor resistance factor (μ) for construction materials, particularly earth-based materials. According to this classification, μ = 1 indicates that the material transmits water vapor as easily as air; μ = 1–10 corresponds to vapor-permeable materials, μ = 10–50 to moderately permeable materials, and μ > 100 to vapor-impermeable materials.

(3) The standards UNE-EN 1504-2:2005 [93], and DIN 4108-3:2024-03 [94], also provide criteria for performance classification. The former defines three categories: Class I—vapor-permeable (S_d < 5 m), Class II (5–50 m), and Class III—vapor-impermeable (S_d > 50 m). The latter standard provides a more detailed classification: vapor-permeable ($S_d \leq 0.5$ m), vapor-retarding (0.5–10 m), vapor-inhibiting (10–100 m), vapor-blocking (100–1500 m), vapor-tight ($S_d \geq 1500$ m).

The experimental results of water vapor permeability tests are summarized in Table 4. An increase in the total vapor flux through the sample (G) corresponds to a proportional increase in the vapor flux per unit area (g) and consequently in the water vapor permeability (Wp). When water vapor diffuses more readily through the material (i.e., when the vapor diffusivity δ_p is high), the material offers lower resistance to vapor transport (i.e., the vapor resistance factor μ is low). As a result, the material behaves as if it were a thinner layer of air with respect to vapor diffusion, corresponding to a lower equivalent air layer thickness (S_d). In practical terms, materials with higher vapor diffusivity improve the breathability of the building envelope, allowing water vapor to pass through more easily, reducing internal moisture accumulation and minimizing the risk of condensation.

A comparison between samples with the same nanoparticle concentration and the same number of coating applications shows that those containing the O formulation generally exhibit higher W_p values and lower μ and S_d values than their counterparts prepared with the W formulation. This indicates that coatings prepared with medium O are generally more permeable to water vapor than those prepared with medium W. Previous observations showed that coatings produced with medium W tended to be more

homogeneous than those prepared with medium O, which may influence the diffusion of water vapor through the coating layer.

Table 4. Water vapor permeability parameters: G (slope of the linear portion of the Δm (kg) vs. time (s) curve), g (water vapor flux density), W_p (water vapor penetration with respect to partial vapor pressure), δ_p (water vapor permeability with respect to partial vapor pressure), δ_a (air permeability to water vapor), μ (water vapor diffusion resistance factor), S_d (equivalent air layer thickness for water vapor diffusion).

Samples	G (kg/s)	g (kg/m^2·s)	W_p (kg/m^2·s·Pa)	δ_p (kg/m·s·Pa)	δ_a (kg/m·s·Pa)	μ	S_d (m)
C	1.9×10^{-9}	1.5×10^{-6}	1.3×10^{-9}	2.6×10^{-11}	2.0×10^{-10}	8.0	0.16
W-1	1.7×10^{-9}	1.3×10^{-6}	1.1×10^{-9}	2.2×10^{-11}	2.0×10^{-10}	9.2	0.18
W-2	1.5×10^{-9}	1.2×10^{-6}	9.7×10^{-10}	1.9×10^{-11}	2.0×10^{-10}	10.6	0.21
W-3	1.6×10^{-9}	1.2×10^{-6}	1.0×10^{-9}	2.1×10^{-11}	2.0×10^{-10}	9.9	0.20
O-1	1.7×10^{-9}	1.3×10^{-6}	1.1×10^{-9}	2.2×10^{-11}	2.0×10^{-10}	9.2	0.18
O-2	1.9×10^{-9}	1.5×10^{-6}	1.2×10^{-9}	2.4×10^{-11}	2.0×10^{-10}	8.4	0.17
O-3	1.6×10^{-9}	1.3×10^{-6}	1.1×10^{-9}	2.1×10^{-11}	2.0×10^{-10}	9.6	0.19
1% LaFe-W-1	1.8×10^{-9}	1.4×10^{-6}	1.2×10^{-9}	2.3×10^{-11}	2.0×10^{-10}	8.8	0.18
1% LaFe-W-2	1.9×10^{-9}	1.5×10^{-6}	1.2×10^{-9}	2.5×10^{-11}	2.0×10^{-10}	8.2	0.16
1% LaFe-W-3	1.4×10^{-9}	1.1×10^{-6}	8.9×10^{-10}	1.8×10^{-11}	2.0×10^{-10}	11.5	0.23
1% LaFe-O-1	1.9×10^{-9}	1.5×10^{-6}	1.3×10^{-9}	2.5×10^{-11}	2.0×10^{-10}	8.1	0.16
1% LaFe-O-2	1.4×10^{-9}	1.1×10^{-6}	9.0×10^{-10}	1.8×10^{-11}	2.0×10^{-10}	11.3	0.23
1% LaFe-O-3	2.0×10^{-9}	1.6×10^{-6}	1.3×10^{-9}	2.6×10^{-11}	2.0×10^{-10}	7.9	0.16
3% LaFe-W-1	1.9×10^{-9}	1.5×10^{-6}	1.2×10^{-9}	2.5×10^{-11}	2.0×10^{-10}	8.0	0.16
3% LaFe-W-2	1.8×10^{-9}	1.4×10^{-6}	1.2×10^{-9}	2.4×10^{-11}	2.0×10^{-10}	8.3	0.17
3% LaFe-W-3	2.2×10^{-9}	1.8×10^{-6}	1.5×10^{-9}	2.9×10^{-11}	2.0×10^{-10}	6.8	0.14
3% LaFe-O-1	1.9×10^{-9}	1.5×10^{-6}	1.3×10^{-9}	2.5×10^{-11}	2.0×10^{-10}	7.8	0.16
3% LaFe-O-2	2.6×10^{-9}	2.1×10^{-6}	1.7×10^{-9}	3.4×10^{-11}	2.0×10^{-10}	5.7	0.11
3% LaFe-O-3	1.5×10^{-9}	1.2×10^{-6}	9.8×10^{-10}	2.0×10^{-11}	2.0×10^{-10}	10.0	0.20
5% LaFe-W-1	2.0×10^{-9}	1.6×10^{-6}	1.3×10^{-9}	2.7×10^{-11}	2.0×10^{-10}	7.3	0.15
5% LaFe-W-2	2.1×10^{-9}	1.7×10^{-6}	1.4×10^{-9}	2.8×10^{-11}	2.0×10^{-10}	7.1	0.14
5% LaFe-W-3	1.9×10^{-9}	1.5×10^{-6}	1.2×10^{-9}	2.5×10^{-11}	2.0×10^{-10}	7.9	0.16
5% LaFe-O-1	1.8×10^{-9}	1.4×10^{-6}	1.2×10^{-9}	2.3×10^{-11}	2.0×10^{-10}	8.4	0.17
5% LaFe-O-2	4.0×10^{-9}	3.2×10^{-6}	2.6×10^{-9}	5.2×10^{-11}	2.0×10^{-10}	3.7	0.07
5% LaFe-O-3	1.8×10^{-9}	1.4×10^{-6}	1.2×10^{-9}	2.3×10^{-11}	2.0×10^{-10}	8.5	0.17

Increasing the number of coating applications does not always result in higher permeability. In general, increasing the $LaFeO_3$ content in coatings prepared with the O medium tends to increase permeability, whereas in coatings prepared with the W medium the effect is less pronounced and may even lead to a slight reduction in permeability.

Considering the experimental values obtained (W_p = 10^{-10}–10^{-9} kg/m^2·s·Pa, μ = 3.7–11.5, and S_d = 0.07–0.23 m), it can be concluded that most of the samples are vapor-permeable, ensuring the breathability of the adobe substrate. From the perspective of the water vapor diffusion resistance factor (μ, dimensionless), only W-2 (10.6), 1% LaFe-W-3

(11.5), and 1% LaFe-O-2 (11.3) exceed the value of 10, with such a small difference that, in practice, they can be considered vapor-permeable rather than moderately permeable (range 10–50). Regarding the equivalent air layer thickness for water vapor diffusion (Sd, m), all samples meet the criterion $S_d \leq 0.5$ m (vapor-permeable). As for water vapor penetration (W_p, kg/m^2·s·Pa), the minimum value was 8.9×10^{-10} kg/m^2·s·Pa (1% LaFe-W-3) and the maximum value was 2.6×10^{-9} kg/m^2·s·Pa (5% LaFe-O-2), corresponding to 1.56 perms and 4.55 perms, respectively; all values fall within the 1.0–10 perms range, corresponding to semi-permeable.

A comparison with the study by Calatan et al. [95], in which adobe bricks were treated with natural protective systems such as linseed oil, beeswax dissolved in oil, and beeswax dissolved in siccative linseed oil, highlights the effectiveness of the coatings developed in the present work in preserving surface breathability. In the aforementioned study, the application of natural waxes and oils led to a substantial increase in the water vapor resistance factor relative to untreated adobe, with values rising by a factor of 1.8 to 2.9, i.e., approximately a two- to threefold increase in resistance to vapor transmission. By contrast, in the present study, the maximum experimentally determined increase factor was 1.44 (sample 1% LaFe-W-3), and a significant proportion of treated samples exhibited negligible changes in water vapor permeability.

Table 5 presents the results obtained from the Karsten tube penetration tests. The control samples were the only ones showing absorption values higher than 3 mL within 10 min, corresponding to very high permeability. This confirms that unprotected adobe is highly vulnerable to the penetration of both water and oils. Adobe blocks coated with formulation W exhibited lower water absorption than those treated with formulation O, confirming the stronger water-repellent capacity of the W formulation. In contrast, for the oil tests, the opposite trend is observed, indicating the higher oleophobicity of coatings prepared with formulation O.

Overall, the application of coatings significantly reduced the permeability of the adobe substrates to both water and the two tested oils. After the first coating application, most samples fell within the low permeability range for water and the relative impermeability range for both oils. Following the second application, samples remained within the low permeability range for water while reaching the no capillary activity/impermeable range for oils. After the third application, the coatings maintained low permeability for water and reached the no capillary activity range for oils. Samples falling outside these ranges generally exhibited lower permeability values as additional coating layers were applied. No significant differences were observed between the two oils. A slight improvement in oleophobicity was detected when using sunflower oil, which should be interpreted as experimental variability related to minor rheological and wetting differences, rather than as evidence of distinct chemical interactions with the coating.

When the $LaFeO_3$ content increased from 1% to 3%, a general decrease in liquid absorption was observed for all three liquids. However, increasing the content to 5% resulted in higher absorption values. As previously discussed, the coatings were not completely homogeneous, and the nanoparticles exhibited a tendency to agglomerate. At lower concentrations, nanoparticles may promote partial pore filling and blockage of capillary pathways, thus hindering liquid penetration. At higher loadings, however, particle agglomeration may create discontinuities withing the coating, facilitating liquid transport.

Table 5. Permeability values against various liquids obtained using the Karsten tube (The footnote indicates the meaning of the colors in terms of permeability).

Samples	**Water Permeability Estimation (mL)**	**$R_{water-water}$**	**Samples**	**Water Permeability Estimation (mL)**	**$R_{water-water}$**	**Samples**	**Water Permeability Estimation (mL)**	**$R_{water-water}$**
C	>3	No	C	>3	No	C	>3	No
W-1	0.42	1	W-2	0.11	1	W-3	0.09	1
O-1	0.69	1	O-2	0.46	1	O-3	0.11	1
1% LaFe-W-1	0.81	1	1% LaFe-W-2	0.51	1	1% LaFe-W-3	0.36	1
1% LaFe-O-1	0.84	1	1% LaFe-O-2	0.53	1	1% LaFe-O-3	0.40	1
3% LaFe-W-1	0.63	1	3% LaFe-W-2	0.19	1	3% LaFe-W-3	0.14	1
3% LaFe-O-1	0.79	1	3% LaFe-O-2	0.51	1	3% LaFe-O-3	0.41	1
5% LaFe-W-1	1.02	1	5% LaFe-W-2	0.87	1	5% LaFe-W-3	0.79	1
5% LaFe-O-1	1.24	1	5% LaFe-O-2	1.04	1	5% LaFe-O-3	0.92	1
Samples	Olive oil permeability estimation (mL)	$R_{olive\ oil-water}$	Samples	Olive oil permeability estimation (mL)	$R_{olive\ oil-water}$	Samples	Olive oil permeability estimation (mL)	$R_{olive\ oil-water}$
C	>3	No	C	>3	No	C	>3	No
W-1	0.54	1.29	W-2	0.24	2.24	W-3	0.13	1.47
O-1	0.32	0.46	O-2	0.07	0.14	O-3	0.05	0.43
1% LaFe-W-1	0.43	0.53	1% LaFe-W-2	0.26	0.50	1% LaFe-W-3	0.16	0.43
1% LaFe-O-1	0.40	0.47	1% LaFe-O-2	0.18	0.33	1% LaFe-O-3	0.08	0.19
3% LaFe-W-1	0.25	0.39	3% LaFe-W-2	0.09	0.45	3% LaFe-W-3	0.08	0.56
3% LaFe-O-1	0.11	0.14	3% LaFe-O-2	0.08	0.15	3% LaFe-O-3	0.03	0.06
5% LaFe-W-1	0.40	0.39	5% LaFe-W-2	0.19	0.21	5% LaFe-W-3	0.11	0.13
5% LaFe-O-1	0.36	0.29	5% LaFe-O-2	0.13	0.12	5% LaFe-O-3	0.06	0.06

Table 5. *Cont.*

Samples	**Water Permeability Estimation (mL)**	**$R_{water-water}$**	**Samples**	**Water Permeability Estimation (mL)**	**$R_{water-water}$**	**Samples**	**Water Permeability Estimation (mL)**	**$R_{water-water}$**
Samples	Sunflower oil permeability estimation (mL)	$R_{sunflower\ oil-water}$	Samples	Sunflower oil permeability estimation (mL)	$R_{sunflower\ oil-water}$	Samples	Sunflower oil permeability estimation (mL)	$R_{sunflower\ oil-water}$
C	>3	No	C	>3	No	C	>3	No
W-1	0.54	1.30	W-2	0.25	2.33	W-3	0.15	1.71
O-1	0.31	0.44	O-2	0.06	0.12	O-3	0.04	0.33
1% LaFe-W-1	0.43	0.53	1% LaFe-W-2	0.27	0.52	1% LaFe-W-3	0.16	0.44
1% LaFe-O-1	0.39	0.46	1% LaFe-O-2	0.16	0.29	1% LaFe-O-3	0.07	0.16
3% LaFe-W-1	0.21	0.33	3% LaFe-W-2	0.09	0.45	3% LaFe-W-3	0.08	0.56
3% LaFe-O-1	0.10	0.12	3% LaFe-O-2	0.07	0.13	3% LaFe-O-3	0.03	0.06
5% LaFe-W-1	0.26	0.26	5% LaFe-W-2	0.19	0.22	5% LaFe-W-3	0.11	0.14
5% LaFe-O-1	0.13	0.10	5% LaFe-O-2	0.12	0.11	5% LaFe-O-3	0.05	0.05

Very high permeability | High permeability | Medium permeability | Low permeability | Relative permeability | Impermeable | No capillary activity

Finally, the oil/water absorption ratios were generally below 1, indicating that oil absorption occurred more slowly than water absorption. This behavior can be attributed to the higher viscosity of oils, which reduces their capillary mobility. Only the W-1, W-2, and W-3 samples exhibited oil–water ratios greater than 1. It should be noted that the W medium is highly water-repellent, while the O medium is hydro-oleophobic. Both formulations therefore act as chemical barriers against liquid penetration, with the W formulation being more effective against water, which explains the higher ratios observed for these samples.

3.5. Durability Tests: Water Immersion and Swinburne Accelerated Erosion Test

The durability tests were designed to evaluate the effectiveness of the coatings in delaying or minimizing the detrimental effects of water on adobe. Two complementary approaches were used: full immersion testing and erosion testing caused by falling water droplets.

Figure 17 presents the results of the water immersion durability test. A comparison between the control sample and the coated specimens clearly shows that the application of both protective media, with or without nanoparticles, significantly increased the resistance time of the adobe bricks under water immersion. Figures 18–21 provide representative examples illustrating the evolution of selected samples, both the control and treated adobe specimens, during immersion in water.

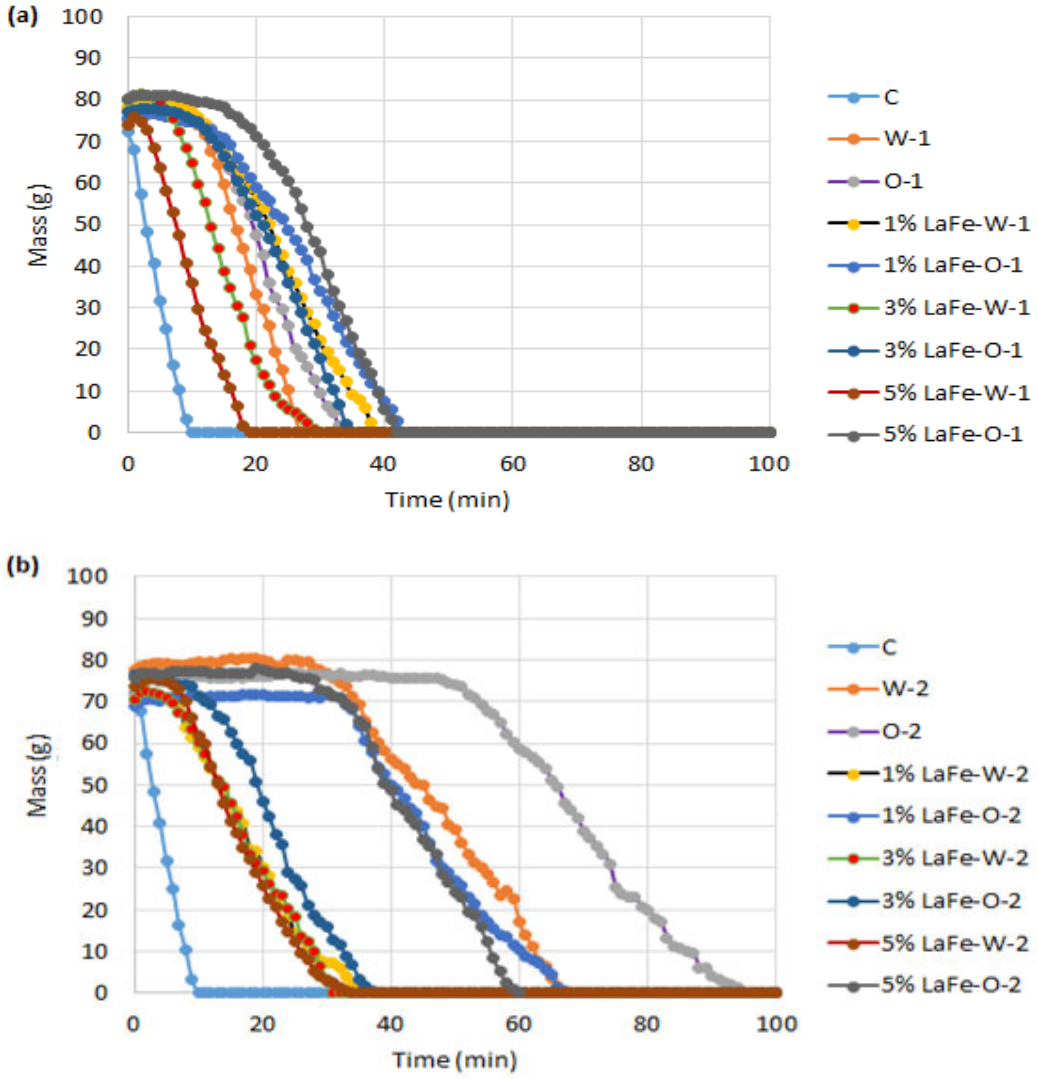

Figure 17. *Cont.*

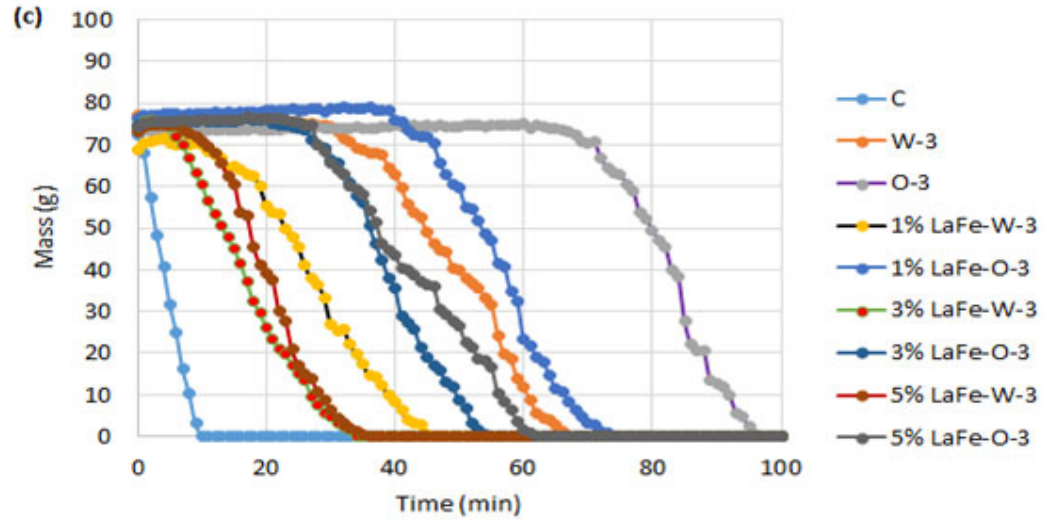

Figure 17. Water immersion durability test results for coatings applied in (**a**) one layer, (**b**) two layers, and (**c**) three layers.

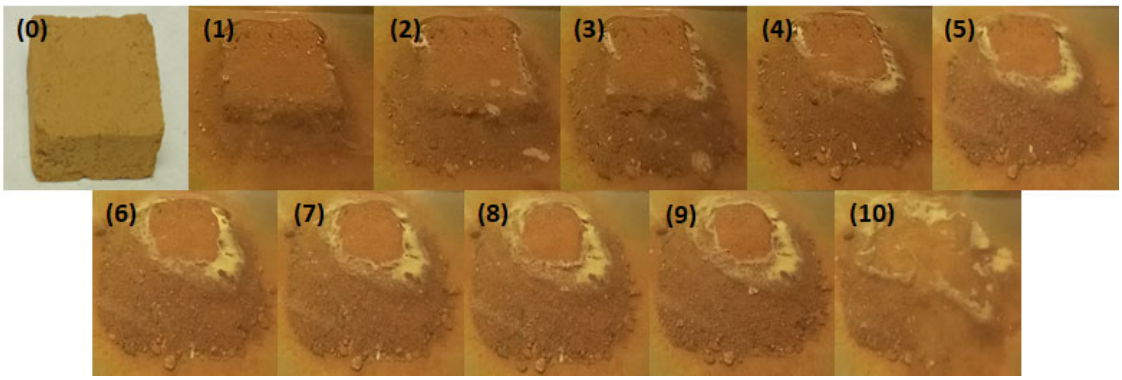

Figure 18. Water immersion durability test on the control sample (immersion time in minutes indicated in parentheses).

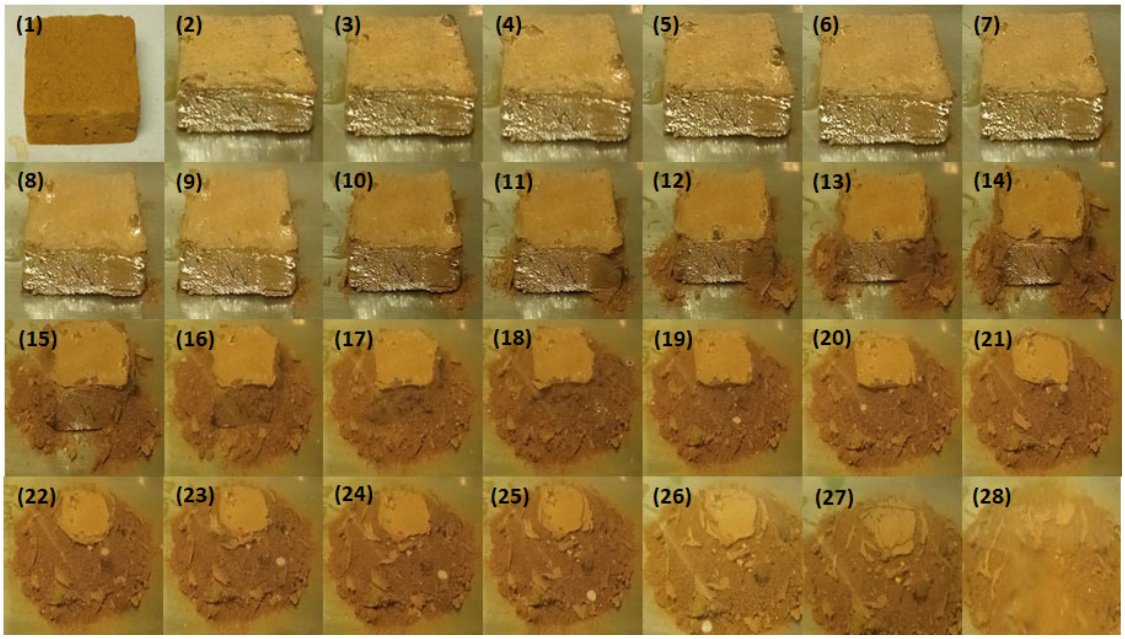

Figure 19. Water immersion durability test of the W-1 sample (immersion time in minutes indicated in parentheses).

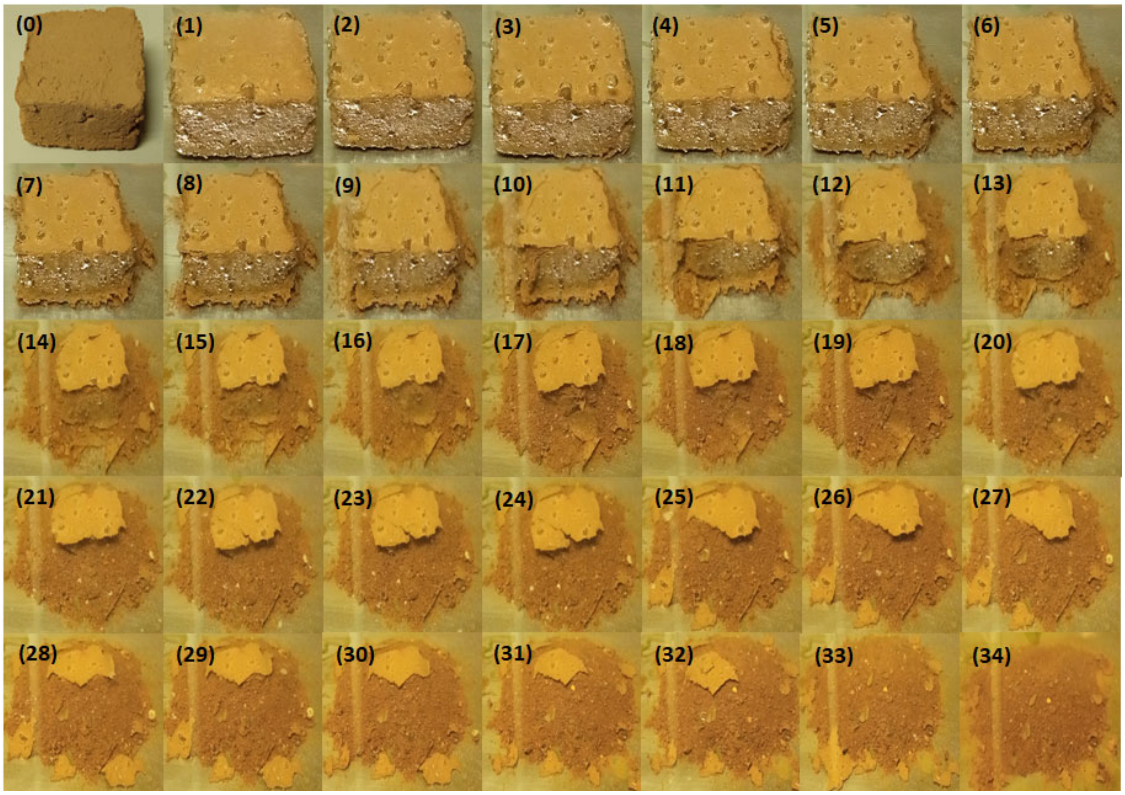

Figure 20. Water immersion durability test of the O-1 sample (immersion time in minutes indicated in parentheses).

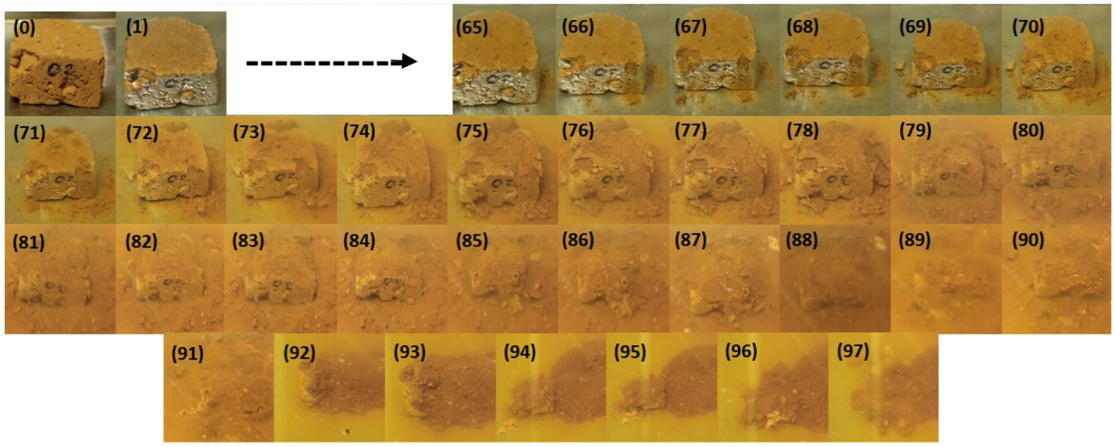

Figure 21. Water immersion durability test of the O-3 sample (immersion time in minutes indicated in parentheses).

All coated samples exhibited an initial increase in mass, which indicates some degree of water absorption at the beginning of the experiment. In contrast, the control sample showed an immediate and continuous loss of mass, as expected, since it was the only specimen not protected by any coating.

A notable increase in the survival time of the specimens was observed when moving from a single coating application to multiple coating layers, demonstrating the beneficial effect of repeated applications in improving water resistance. However, the presence of nanoparticles generally resulted in a slight reduction in durability compared with coatings without nanoparticles. This behavior may be related to the well-known tendency of $LaFeO_3$ nanoparticles to agglomerate. Such agglomeration could create additional

hydrophilic sites or structural discontinuities within the coating, partially counteracting its hydrophobic properties.

The results of the Swinburne Accelerated Erosion Test (SAET) are presented in Table 6 and Figure 22. Table 6 reports the mass loss of the adobe specimens as well as the presence or absence of cavities generated by erosion due to falling water droplets. Figure 22 provides visual evidence of this deterioration.

Table 6. Mass loss (%) and cavity depth (mm) obtained from Swinburne Accelerated Erosion Test (SAET).

Samples	Mass Loss (%)	Cavity Presence
C	79.0	-
W-1	5.3	YES
W-2	1.4	YES
W-3	0.4	-
O-1	2.2	-
O-2	0.3	-
O-3	0.1	-
1% LaFe-W-1	1.5	YES
1% LaFe-W-2	4.6	-
1% LaFe-W-3	1.6	-
1% LaFe-O-1	1.7	-
1% LaFe-O-2	0.3	-
1% LaFe-O-3	0.9	-
3% LaFe-W-1	10.3	YES
3% LaFe-W-2	2.5	YES
3% LaFe-W-3	1.5	-
3% LaFe-O-1	0.7	-
3% LaFe-O-2	0.4	-
3% LaFe-O-3	0.1	-
5% LaFe-W-1	16.4	YES
5% LaFe-W-2	1.1	-
5% LaFe-W-3	1.0	-
5% LaFe-O-1	1.2	-
5% LaFe-O-2	0.1	-
5% LaFe-O-3	1.6	YES

The control sample experienced severe erosion that ultimately led to its destruction. This outcome was expected, as adobe is known to be highly susceptible to water-induced erosion, particularly when no protective coating is applied. In contrast, the application of either hydrophobic (W) or hydro-oleophobic (O) media significantly reduced the extent of erosion. Consistent with the observations from the immersion tests, increasing the number of coating layers improved protection against water, generally resulting in lower mass loss and the absence of erosion cavities.

However, the presence of $LaFeO_3$ nanoparticles introduced additional effects. These particles tend to agglomerate, forming larger aggregates that increase the surface area exposed to water, thereby promoting water-surface interaction and potentially accelerating

material erosion. This effect may be further amplified by the lower homogeneity observed in some coatings, which could explain the non-linear variation in mass loss.

For samples prepared with the W formulations, the formation of erosion cavities suggests a reduced ability of the coating to dissipate or redistribute the kinetic energy of the impacting droplets, leading to localized fatigue and particle detachment. The wear observed in these samples was therefore not related to a lower water-repellent capacity, since formulation W is more hydrophobic than O, but rather to a lower capacity to dissipate the mechanical energy of droplet impacts. Although droplets may partially rebound from the surface, part of their kinetic energy is transmitted to the substrate, generating microfractures that progressively contribute to material erosion, a behavior consistent with the formation and propagation of fractures reported in aging protective coatings [96].

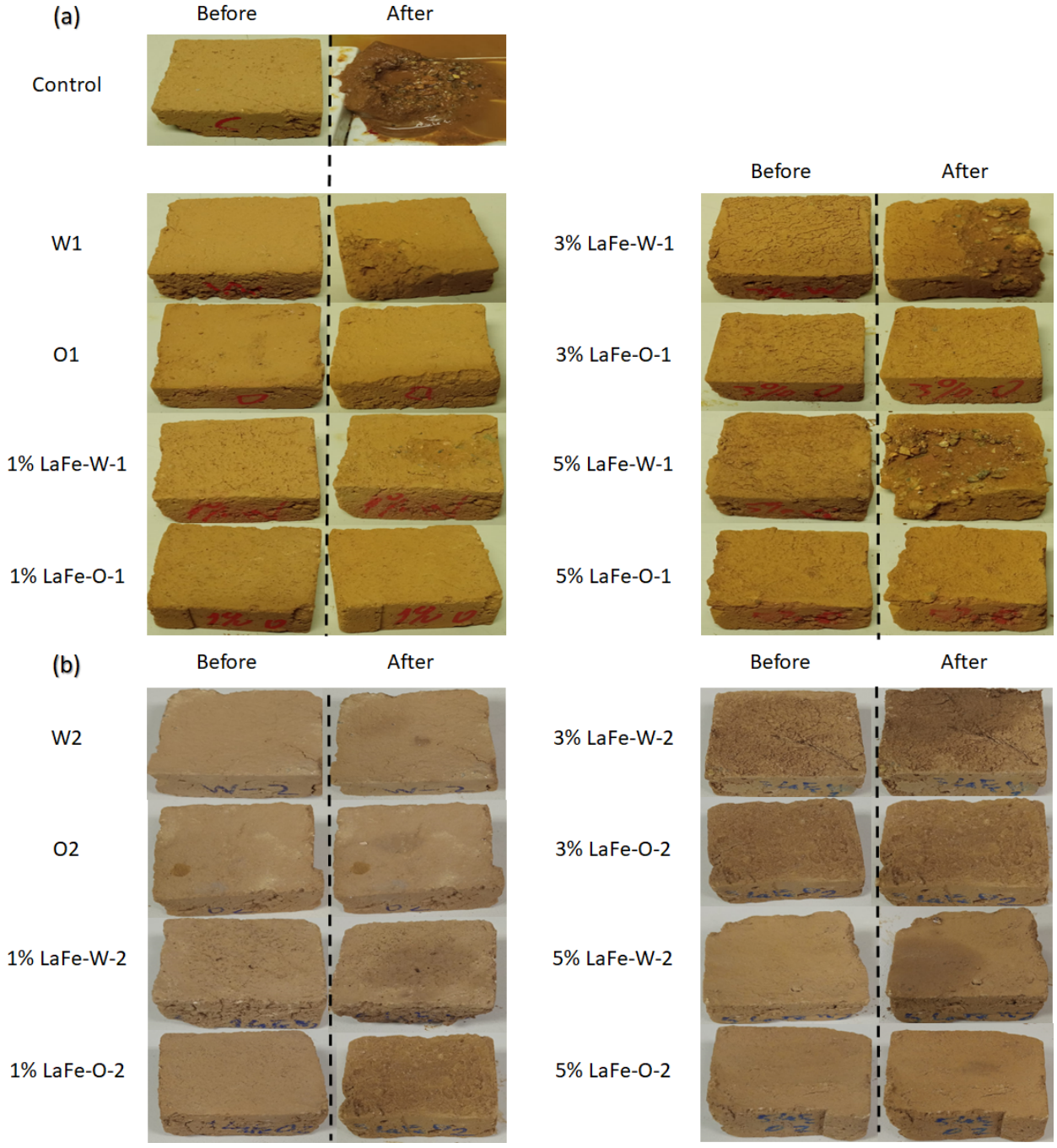

Figure 22. *Cont.*

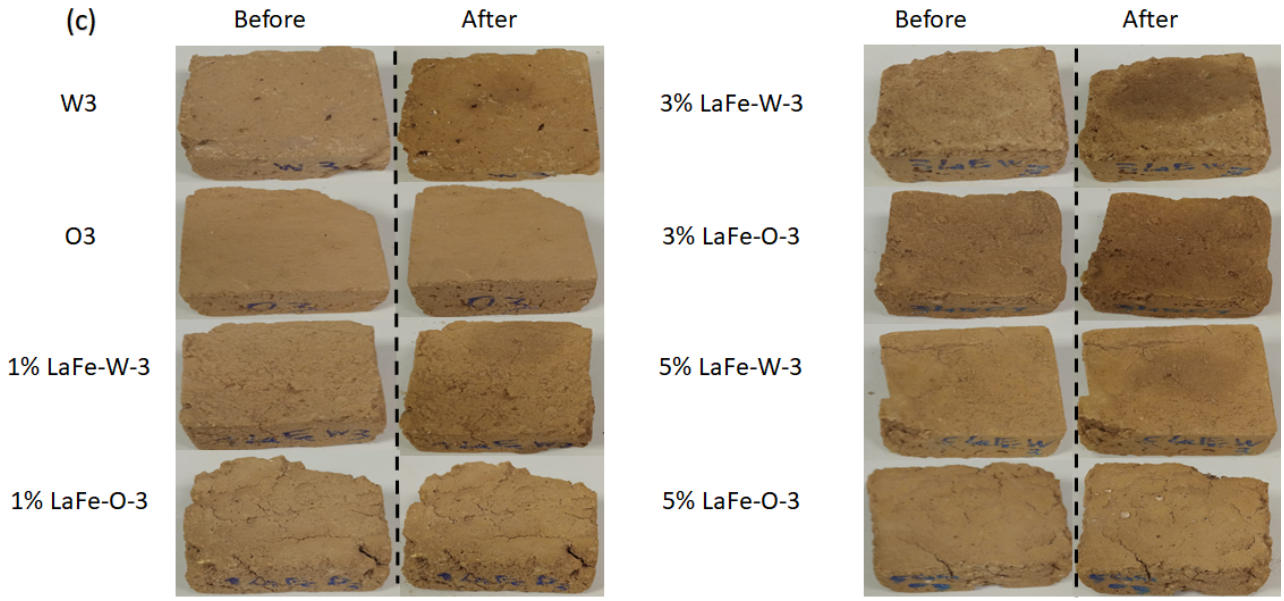

Figure 22. Visual comparison of adobe samples before and after SAET: (**a**) control and single coating application, (**b**) double coating application, and (**c**) triple coating application.

3.6. Photocatalytic Activity Measurements of the Coatings

The photocatalytic efficiency of the coatings for NO_x abatement under solar and strictly visible irradiation is presented in Figure 23a and Figure 23b, respectively. Experimentally, the following average NO and NO_x abatement values were obtained for the catalyst-containing samples: W under solar light (1.71% NO and 0.54% NO_x), O under solar light (2.22% NO and 0.64% NO_x), W under strictly visible light (1.07% NO and 0.36% NO_x), and O under strictly visible light (1.62% NO and 0.58% NO_x). These results indicate slightly higher for coatings prepared with the hydro-oleophobic medium (O). This behavior may be attributed to the lower homogeneity of the O coatings, which creates areas where the active nanoparticles remain partially exposed, rather than being surrounded by the repellent matrix. This increases the number of active contact points with the contaminant, leading to slightly improved photocatalytic performance. The SEM micrographs shown in Figures 11 and 12 support this interpretation, revealing regions where nanoparticles are more exposed to type O-type coatings. Additionally, the porous nature of the adobe substrate, which is more exposed and less uniformly covered in O-type coatings, may facilitate the adsorption of NO molecules, further promoting their degradation.

Regarding the influence of the number of coating applications and nanoparticle content, no clear correlation was observed. In principle, increasing the number of coating layers and/or the percentage of nanoparticles should lead to the incorporation of a greater number of photocatalytic heterostructures. However, higher photocatalyst loadings may also enhance particle agglomeration, which can reduce photocatalytic efficiency due to coupling and hole-electron deactivation, as reported in the literature [97].

Overall, the samples incorporating $LaFeO_3$ nanoparticles showed measurable photocatalytic activity compared to those without photocatalyst, although the activity was not particularly pronounced. Although the recorded values were lower than those reported for other photocatalysts in previous studies [36,40], where highly active and well-established systems such as TiO_2 or heterostructures incorporating ZnO in addition to titania were employed, the objective of this work was not to maximize photocatalytic activity. Instead, priority was given to preserving the characteristic dark colour of adobe by selecting a Fe-based photocatalyst. This choice was made because photocatalysts such as those mentioned above are known to induce an undesirable bleaching effect on the surface.

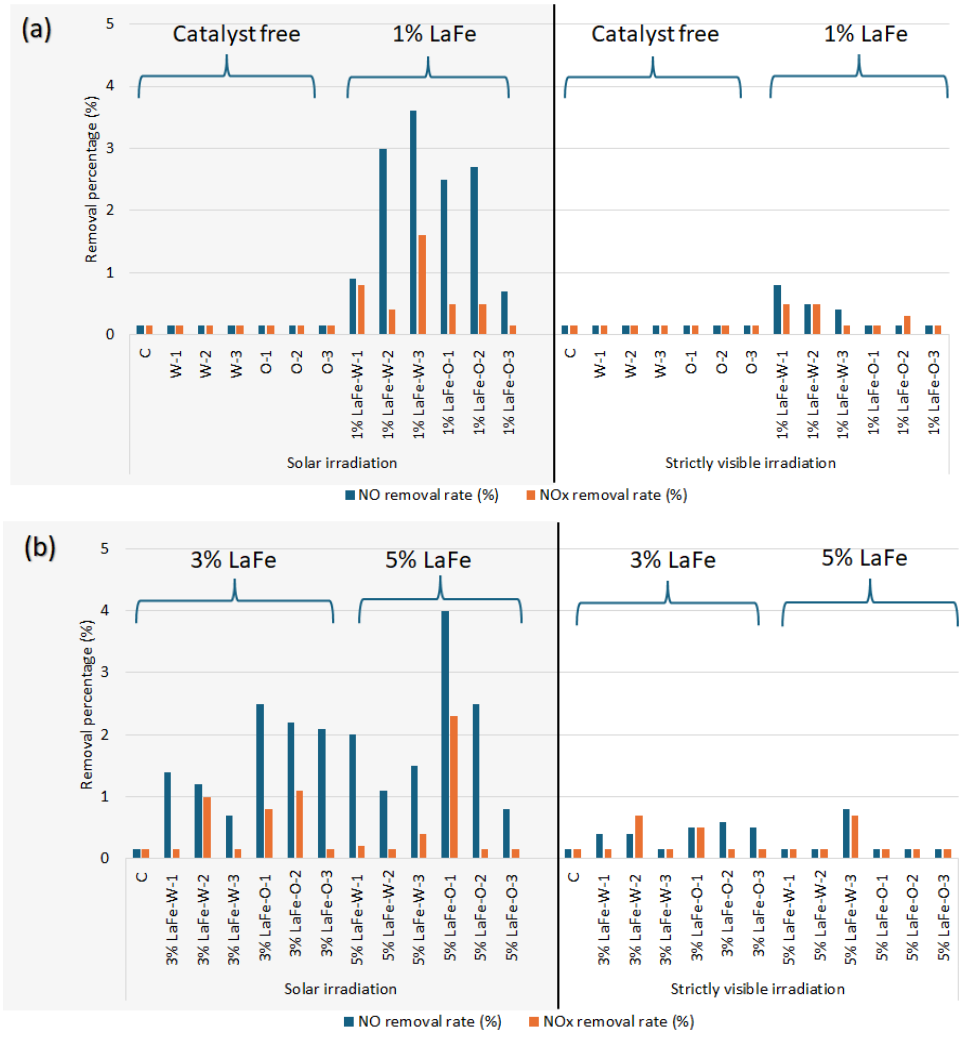

Figure 23. Photocatalytic NO and NO_x removal efficiencies of LaFe coatings: (**a**) control, carrier media and 1% LaFe; (**b**) control, 3% LaFe and 5% LaFe.

The value obtained can be correlated with several factors. First, the intrinsic activity of non-doped and non-thermally activated $LaFeO_3$ perovskite is relatively limited. Measurements of the pure photocatalyst showed that the performance of the pure photocatalyst did not exceed 20% NO removal (with a maximum NO_x removal of 14%) under solar irradiation. These results were consistent with values reported in the literature, such as phenol degradation of approximately 30% [85] and methane conversion at low temperatures in the range of 10–20% [86]. Second, the photocatalyst loading in the coatings was relatively low (1%, 3%, and 5% w/v), which limited the number of available active sites for photocatalytic reactions. Third, microstructural analysis revealed a tendency of the photocatalytic nanoparticles to agglomerate and become partially embedded in the matrix formed by the carrier medium, further reducing their accessibility and contributing to the limited photocatalytic performance observed.

Consistent with previous studies [39,43], higher removal efficiencies were obtained under solar irradiation (combined ultraviolet-visible light) than under strictly visible light. Ultraviolet (UV) radiation provides photons with sufficient energy to promote electrons from the valence band to the conduction band through band-to-band excitation. In contrast, visible light often lacks the required photon energy to overcome the band gap, particularly in unmodified materials. Consequently, UV irradiation generates a higher density of electron–hole pairs, thereby enhancing photocatalytic activity. Moreover, UV light can induce direct band-to-band electronic transitions, whereas visible light typically activates

only intermediate energy levels or defect states, when present. Under combined UV and visible irradiation, such as that provided by the solar spectrum, multiple excitation pathways may occur simultaneously, resulting in improved overall photocatalytic activity.

A comparative analysis of the band gap energies of various photocatalysts—namely TiO_2–ZnO (3.08 eV) [43] and Bi_2O_3–ZnO (2.99 eV) [43]—indicates that $LaFeO_3$ (2.34 eV) [98] exhibits the greatest responsiveness to visible light irradiation. Nevertheless, this apparent advantage does not directly correlate with enhanced photocatalytic activity. Electron paramagnetic resonance (EPR) studies [43] reveal that TiO_2–ZnO and Bi_2O_3–ZnO systems promote the efficient formation of hydroxyl and superoxide radicals, whereas $LaFeO_3$ demonstrates comparatively lower radical generation and less efficient electron–hole separation [99,100].

Therefore, although $LaFeO_3$ demonstrates enhanced visible-light absorption, its photocatalytic efficiency is likely limited by rapid electron–hole recombination, which reduces the formation of reactive species involved in NO_x degradation. Further research on lanthanum-based perovskites is needed to overcome these limitations.

Finally, it should be noted that the potential chemical changes in the coatings induced by prolonged light exposure were not specifically addressed in this study. Although the photocatalytic performance under solar and visible irradiation was evaluated, further investigation would be required to assess the long-term chemical stability of the coatings and possible photo-induced transformations under environmental conditions. This aspect will be considered in future work.

3.7. Life Cycle Costing (LCC) and Life Cycle Assessment (LCA)

Figure 24 presents the results for costs, energy consumption, and CO_2 emissions obtained from Life Cycle Costing (LCC) and Life Cycle Assessment (LCA) analysis. The comparison is made between the control case building (used as the baseline scenario) and the same building in which the reinforced concrete walls are replaced by adobe bricks prepared on site from excavated soil, whose durability is ensured by the application of protective coatings (W and O) containing $LaFeO_3$ photocatalytic nanoparticles (5%).

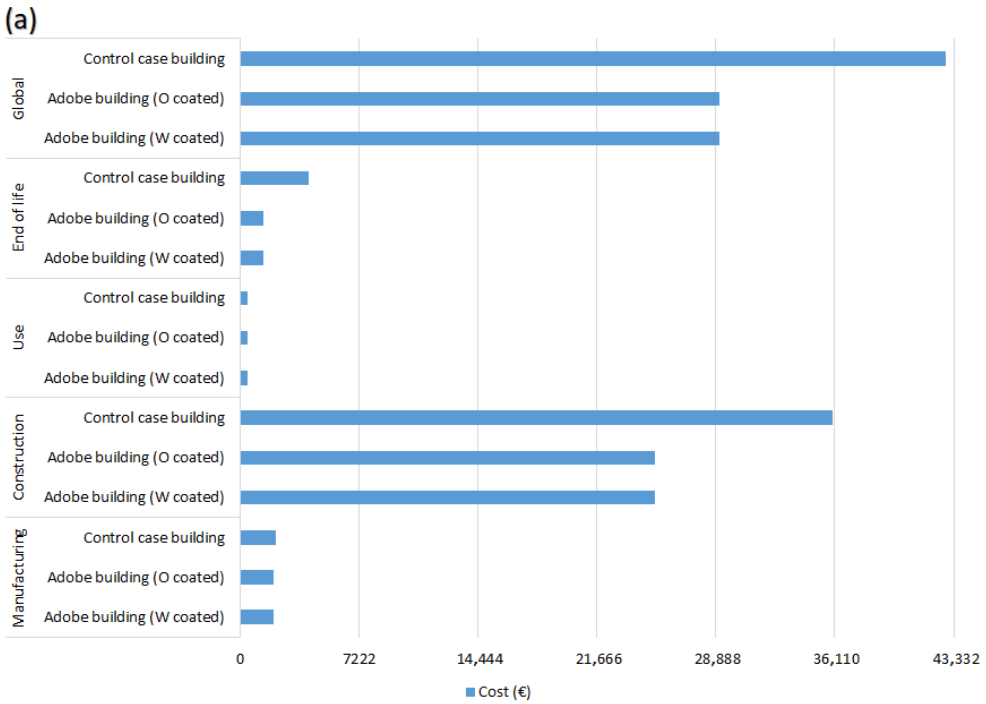

Figure 24. *Cont.*

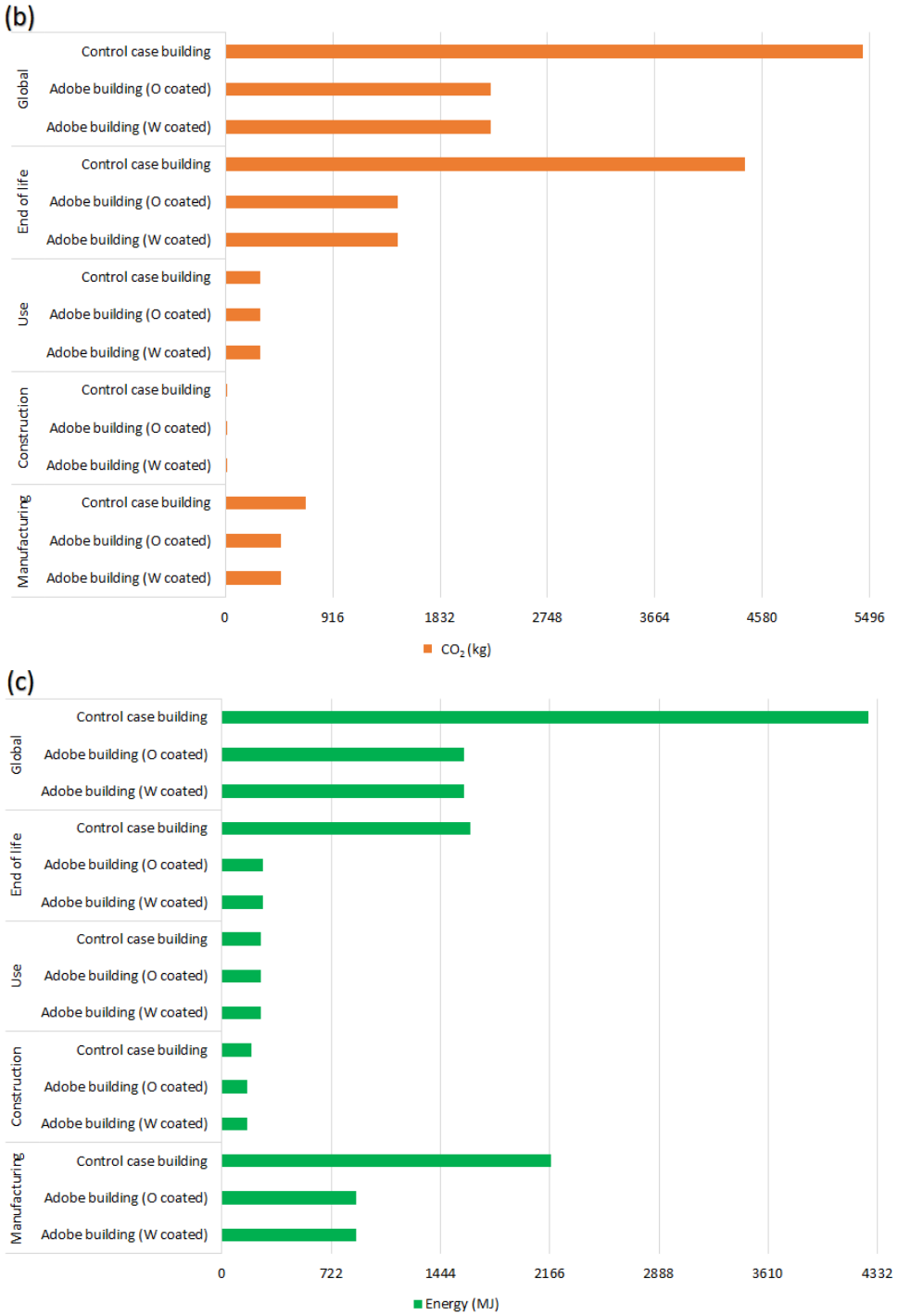

Figure 24. Life Cycle Costing (LCC) and Life Cycle Assessment (LCA) results for the control case building and adobe buildings with 5% LaFe-W and 5% LaFe-O coatings: (**a**) cost, (**b**) energy consumption, and (**c**) CO_2 emissions.

The construction phase represents the highest cost, which is consistent with expectations, as labor and material procurement generally account for a substantial proportion of total expenditures. Both coatings (W and O) exhibit identical values during the use phase, since they involve standardized activities, mainly labor and transport. Similarly, the end-of-life stage of the adobe building shows identical values for both coatings, reflecting the fact that demolition and waste management processes are primarily determined by the built floor area, regardless of the coating type.

From the perspective of CO_2 emissions, the end-of-life stage is the most polluting phase, followed at a considerable distance by the manufacturing stage. This is mainly due to the inclusion of demolition operations and waste management processes in the end-of-life stage, whereas manufacturing includes the production of construction materials and finishing products. In terms of energy demand, the manufacturing stage is the most energy-intensive, since it encompasses both material production and finishing processes. The construction stage also requires a significant amount of energy due to the operation of machinery and labor-related activities.

It should also be noted that several materials used in the control case building were replaced with adobe bricks, thereby eliminating the need for crushing processes during the end-of-life stage. Consequently, the end-of-life phase is significantly more energy-intensive in the control case building than in the adobe-based alternative.

The comparison between the control case building and the adobe-based house demonstrates that the use of adobe produced in situ from excavated soil significantly reduces costs, CO_2 emissions associated with transport and industrial material production, and the energy required during construction. For example, when compared with the most expensive and polluting coating scenario (5% LaFe-O), the adobe-based solution achieves a 32% reduction in costs, a 58% reduction in CO_2 emissions, and a 63% reduction in energy consumption. However, it is true that the absence of experimental validation or real-world industrial datasets may introduce uncertainties in the results. Consequently, these findings should be further evaluated and adapted to practical applications, taking into account all verified numerical data.

Selected modifications were introduced in two of the fixed parameters to evaluate their influence on the final outcomes. In particular, the coating lifetime was adjusted by assuming the absence of maintenance and reapplication, thereby extending it to 25 years instead of 10. Additionally, the distance to the companies responsible for the production and supply of raw materials was reduced to 12 km instead of 30. Accordingly, three scenarios were considered: (i) the original 5% LaFe–O system, (ii) 5% LaFe–O with a 2.5-fold increase in coating lifetime, and (iii) 5% LaFe–O with a 2.5-fold reduction in transportation distance.

The baseline scenario yielded 32% cost savings, a 58% reduction in CO_2 emissions, and 63% energy savings. Extending the coating lifetime resulted in 32% cost savings, 60% CO_2 reduction, and 64% energy savings. In contrast, reducing the transportation distance produced 32% cost savings, 61% CO_2 reduction, and 63% energy savings. These findings indicate that controlled variations of equivalent magnitude in coating lifetime and transport distance exert comparable effects on the evaluated performance metrics. Nevertheless, in practical applications, a detailed case-specific assessment would be required to appropriately define these parameters.

These results highlight the considerable potential of raw earth construction materials, particularly when their durability is enhanced through protective multifunctional coatings, from both economic and environmental perspectives. This is especially relevant considering that adobe construction is an ancient technique requiring minimal technological infrastructure and relatively low costs, making it particularly suitable for new buildings in developing regions.

It should also be noted that the main difference between the two buildings analyzed lies in the wall materials, both exterior and interior. In building designs where a greater proportion of materials are replaced by adobe or other earthen construction materials, even greater improvements could be achieved in terms of lower energy consumption, reduced costs, and decreased CO_2 emissions.

Finally, the development of advanced technologies such as robotics, intelligent materials, and artificial intelligence may further reduce the number of workers and construction

time, which would positively influence energy consumption, costs, and associated CO_2 emissions. As new construction techniques and multifunctional materials with properties such as hydrophobicity, oleophobicity, self-cleaning ability, and photocatalytic activity continue to evolve, the costs of raw material production and the associated environmental impacts are expected to decrease while overall performance improves.

4. Conclusions

Multifunctional coatings were successfully developed by incorporating photocatalytic $LaFeO_3$ nanoparticles into highly water-repellent (W) and hydro-oleophobic (O) three-dimensional matrices. These coatings were applied to adobe, a traditional construction material that has recently attracted renewed attention due to its low environmental impact and sustainability potential.

The distribution of the coatings on the adobe substrates was found to be non-uniform, mainly due to the inherent surface irregularity and porosity of adobe. The highly hydrophobic (W) formulations achieved greater surface coverage and more homogeneous distribution, whereas hydro-oleophobic (O) formulations showed poorer dispersion and a greater tendency for nanoparticle agglomeration.

The photocatalytic activity of the coatings was relatively limited, which can be attributed to both the moderate intrinsic activity of $LaFeO_3$ and the low nanoparticle loading in the coatings. Although more efficient photocatalysts could potentially enhance performance by synergizing with the porosity and alkalinity of adobe, such materials would likely introduce undesirable color alterations, particularly whitening effects on the surface. Therefore, a balance was established between photocatalytic performance and preservation of the characteristic chromatic appearance of adobe.

Despite the limited number of coating applications, the low nanoparticle content, and the challenging nature of the substrate, both formulations imparted significant liquid-repellent properties. Static contact angle measurements showed values above 90° for both water and oils, with some samples approaching the thresholds of superhydrophobicity (5% LaFe-W-1: 136.2°) and superoleophobicity (5% LaFe-O-1: 135.4°). Overall, the results confirmed the strong repellency of the coatings, with W formulations exhibiting higher hydrophobicity and O formulations providing greater oleophobicity.

Vapor permeability tests indicated acceptable permeability ranges for all coatings, with hydro-oleophobic formulations showing slightly higher permeability. The measured water vapor permeability (10^{-10}–10^{-9} $kg/m^2 \cdot s \cdot Pa$), water vapor diffusion resistance factor (3.7–11.5), and equivalent air layer thicknesses (0.07–0.23 m) confirmed that the coated samples remained vapor-permeable, thus maintaining the breathability of the adobe substrate.

Durability tests, including water immersion, Karsten tube penetration, and the Swinburne Accelerated Erosion Test (SAET), supported the results obtained from the contact angle measurements. The immersion test increased the water resistance time of adobe from approximately 10 min (bare adobe) to nearly 1.5 h (O-3). Karsten tube tests revealed substantial reductions in both water and oil permeability. While bare adobe exhibited absorption values above 3 mL/10 min (very high permeability), the coated samples showed drastically reduced permeability, reaching low permeability or no capillary activity ranges. SAET results further demonstrated the effectiveness of the coatings against erosion caused by repeated water droplet impacts; while bare adobe experienced severe deterioration, coated samples showed limited mass loss and minor or no perforation.

Finally, Life Cycle Assessment (LCA) and Life Cycle Costing (LCC) analyses confirmed the high sustainability potential of adobe construction. The comparison between a 40.3 m^2 dwelling with cast-in-place reinforced concrete walls and a similar dwelling in which the only modification was the replacement of these walls with adobe blocks produced in situ

showed significant improvements, with cost reductions of 32%, CO_2 emission reductions of 58%, and energy savings of 63%.

Overall, these findings highlight the potential of multifunctional protective coatings for enhance the durability of adobe while preserving its environmental advantages, supporting its safe implementation in contemporary construction as well as in the conservation of architectural heritage.

Author Contributions: Conceptualization: V.M.T.-S., J.I.Á., Í.N.-B. and J.M.F.; Methodology: V.M.T.-S., J.I.Á. and Í.N.-B.; Validation: V.M.T.-S.; Formal analysis: V.M.T.-S. and Í.N.-B.; Investigation: V.M.T.-S., J.I.Á. and Í.N.-B.; Resources: J.I.Á. and Í.N.-B.; Data curation: V.M.T.-S.; Writing—original draft preparation: V.M.T.-S.; Writing—review and editing: V.M.T.-S., J.I.Á., J.M.F., L.K. and G.K.; Visualization: V.M.T.-S. and J.I.Á.; Visualization: V.M.T.-S. and J.I.Á.; Supervision: J.I.Á. and Í.N.-B.; Project administration: J.I.Á. and Í.N.-B.; Funding acquisition: J.I.Á. and Í.N.-B. All authors have read and agreed to the published version of the manuscript.

Funding: This work was funded by MICINN/AEI/10.13039/501100011033, through the grants PID2020-119975RB-100 (LIMORTHER) and TED2021-129705B-C33 (Terra-Cycle) and by Gobierno de Navarra, PC142-143 MULTIFICON. Funding was also provided by the European Union's Horizon 2020 research and innovation programme under the Marie Skłodowska-Curie grant agreement no. 101034345. Víctor M. Tena-Santafé thanks the Asociación de Amigos de la Universidad de Navarra, for funding support through a pre-doctoral grant.

Institutional Review Board Statement: Not applicable.

Informed Consent Statement: Not applicable.

Data Availability Statement: The original contributions presented in this study are included in the article. Further inquiries can be directed to the corresponding author.

Acknowledgments: The authors would like to thank Universidad Politécnica de Cataluña for providing soil samples within the framework of the Terra-Cycle Project, which was essential for the completion of this study. ChatGPT (Open AI, GPT-5.3-mini) was used during the preparation of this work only for language improvement purposes. After using this service, the authors reviewed and edited the content as needed and take full responsibility for the content of the published article. Gemini 3 Flash, Web Version (Google, 16 April 2026) was also used for obtaining Figure 1b.

Conflicts of Interest: The authors declare that they have no known competing financial interest or personal relationships that could have appeared to influence the work reported in this paper.

Appendix A

For each weighing series, the accumulated mass variation was calculated using Equation (A1):

$$|\mathbf{\Delta m_i}| = \mathbf{m_i} - \mathbf{m_0} \quad \text{(A1)}$$

where m_i and m_0 are the masses (kg) measured at times t_i and t_0 (s), respectively.

The slope of the linear portion of the G curve (kg/s), representing the mass variation (Δm_i) as a function of time (t), was determined by linear regression using at least five consecutive aligned data points. Once the slope was obtained, the water vapor flux density was calculated using Equation (A2):

$$\mathbf{g} = \mathbf{G}/\mathbf{A} \quad \text{(A2)}$$

where A (m^2) is the test surface area (in this case, a circular area), and g ($kg/m^2 \cdot s$) is the water vapor flux density.

Equation (A3) shows the formula used to calculate water vapor permeability:

$$\mathbf{W_p} = \frac{\mathbf{G}}{\mathbf{A} \times \mathbf{\Delta P_v}} \quad \text{(A3)}$$

where ΔP_v (Pa) is the difference in water vapor pressure, calculated from the average temperature and relative humidity recorded during the test. W_p (kg/m^2·s·Pa) represents the water vapor permeability with respect to the partial vapor pressure.

In this study, the internal zone exhibited a temperature of 23 °C and 93% relative humidity, while the external zone exhibited 23 °C and 50% relative humidity. According to the National Institute of Standards and Technology [54], the saturation vapor pressure of water at 23 °C is 2811 Pa. Multiplying this value by the relative humidity yields 2614 Pa for the internal zone and 1406 Pa for the external zone. The difference between these two values was used as ΔP_v in Equation (A4).

Equation (A4) shows the calculation of water vapor permeability:

$$\delta_p = W_p \cdot D \quad \text{(A4)}$$

where D (m) is the average thickness of the adobe specimen and δ_p (kg/m·s·Pa) represents the water vapor permeability coefficient with respect to the partial vapor pressure.

Equation (A5) is Schirmer's formula:

$$\delta_a = 0.0000231 \times \frac{P_0}{P \times R \times T} \times \left(\frac{T}{273}\right)^{1.81} \quad \text{(A5)}$$

where P_0 is the standard barometric pressure (1013.25 hPa), P (hPa) is the barometric pressure obtained as the average of the values provided by Agencia Estatal de Meteorología (AEMET) during the measurements, T (K) is the temperature, and R (462 Nm/kg·K) is the gas constant for water vapor. The parameter δ_a represents the permeability of air to water vapor (kg/m·s·Pa).

The water vapor diffusion resistance factor (μ) was calculated using Equation (A6):

$$\mu = \frac{\delta_a}{\delta_p} \quad \text{(A6)}$$

Finally, the equivalent air layer thickness for water vapor diffusion was determined using Equation (A7):

$$S_d = \mu \times D \quad \text{(A7)}$$

where S_d (m) is the equivalent air layer thickness for water vapor diffusion.

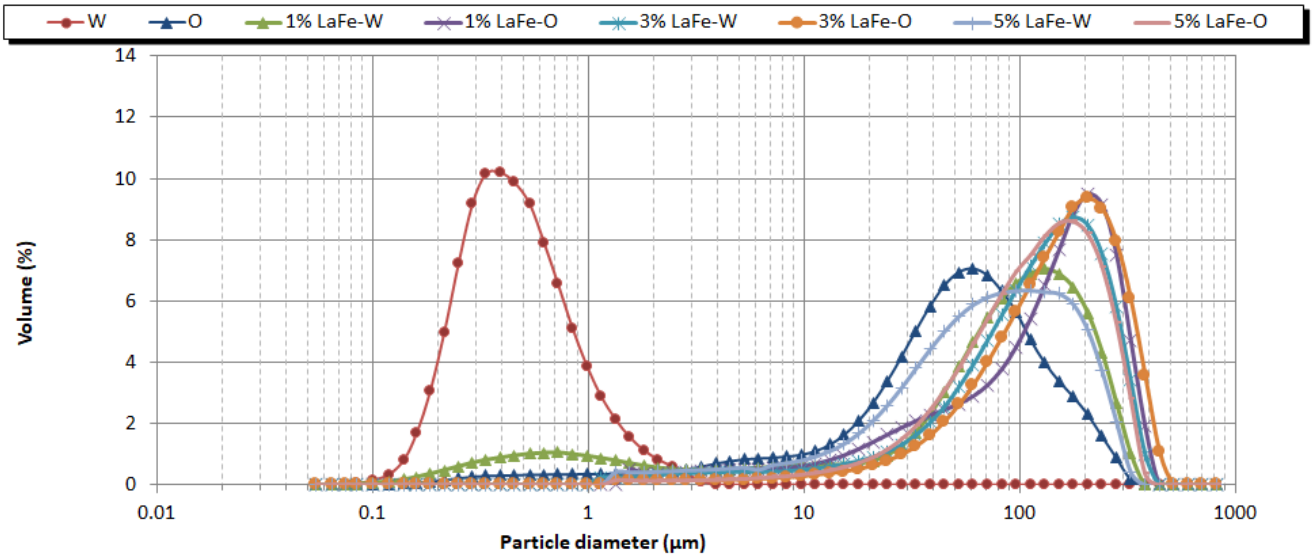

Figure A1. Particle size distribution of $LaFeO_3$ dispersions.

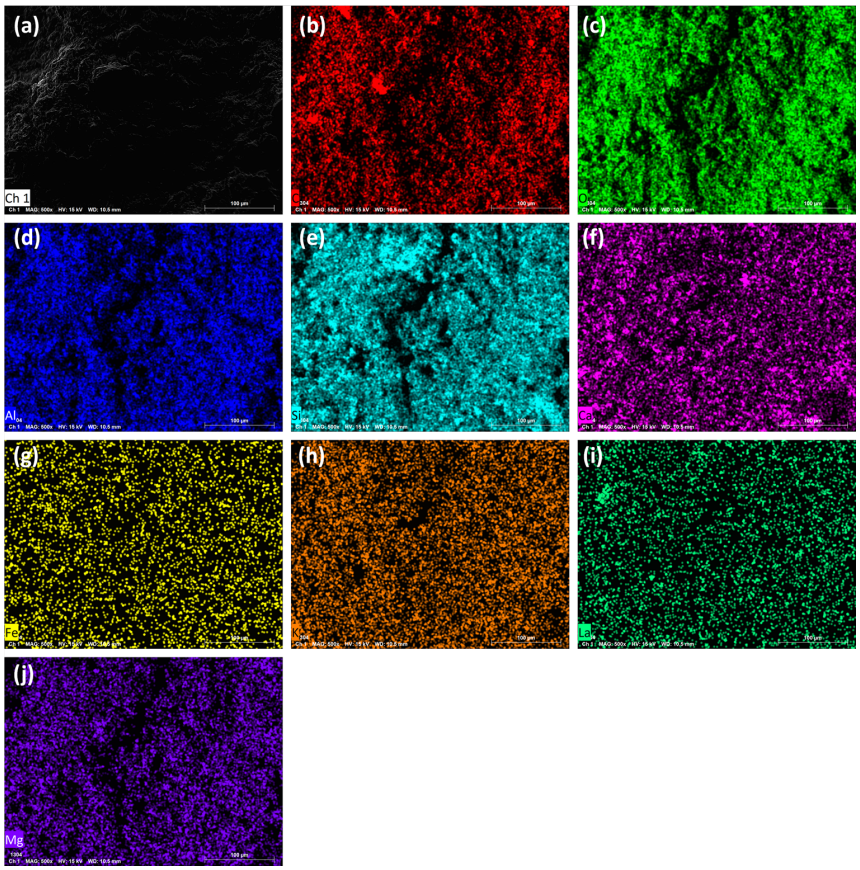

Figure A2. Individual EDS elemental maps for the control sample, where (**a**) Original sample, and distribution maps: (**b**) C, (**c**) O, (**d**) Al, (**e**) Si, (**f**) Ca, (**g**) Fe, (**h**) K, (**i**) La, and (**j**) Mg.

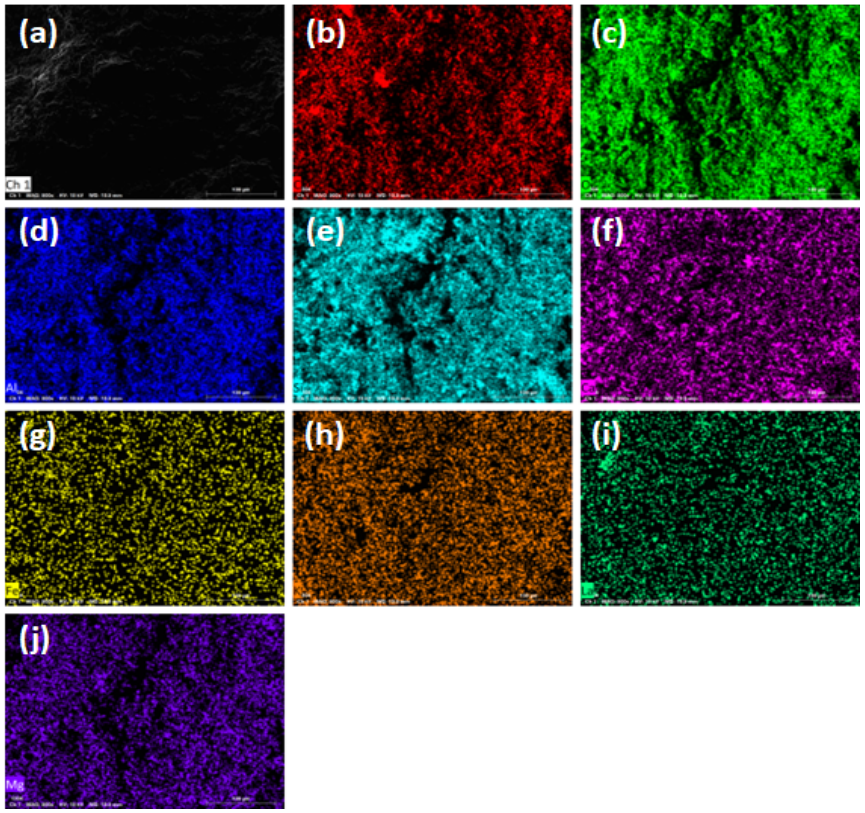

Figure A3. Individual EDS elemental maps for the 1% LaFe-W-1 sample, where (**a**) Original sample, and distribution maps: (**b**) C, (**c**) O, (**d**) Al, (**e**) Si, (**f**) Ca, (**g**) Fe, (**h**) K, (**i**) La, and (**j**) Mg.

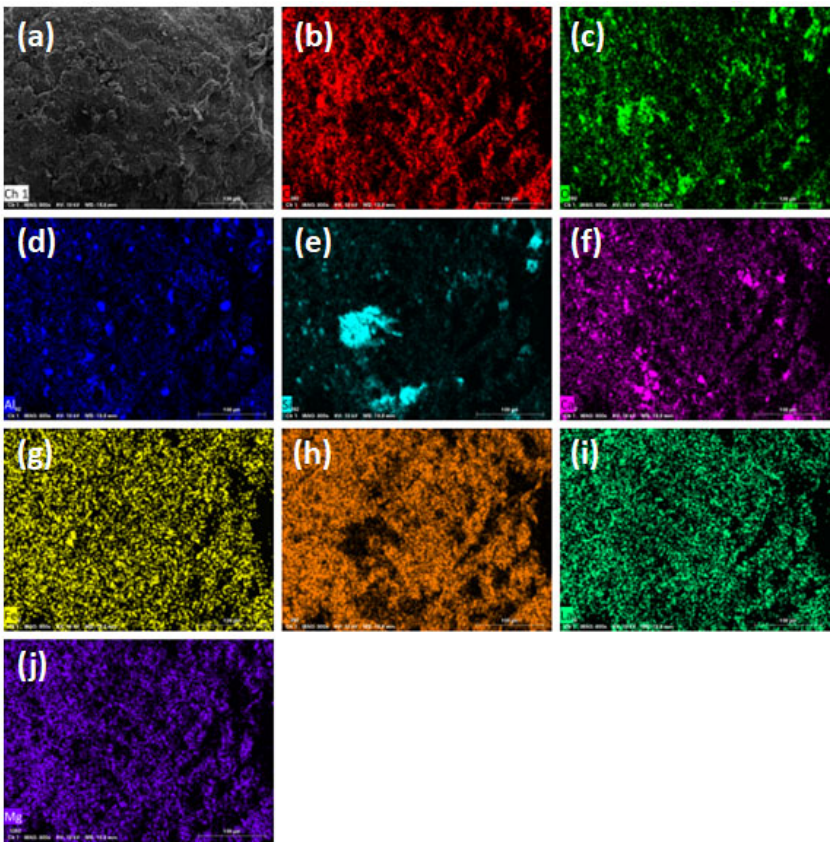

Figure A4. Individual EDS elemental maps for the 1% LaFe-O-1 sample, where (**a**) Original sample, and distribution maps: (**b**) C, (**c**) O, (**d**) Al, (**e**) Si, (**f**) Ca, (**g**) Fe, (**h**) K, (**i**) La, and (**j**) Mg.

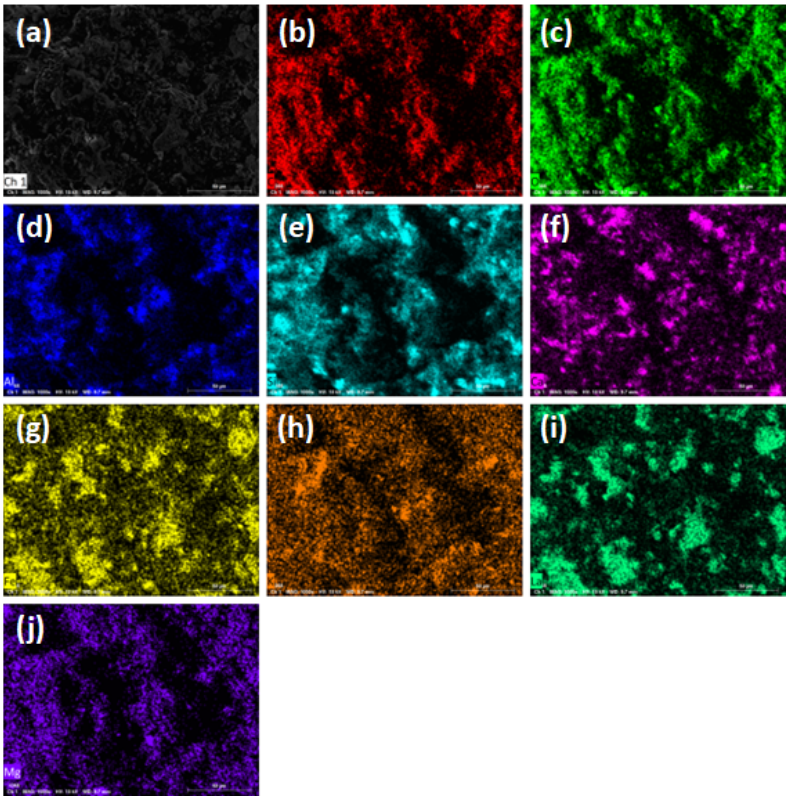

Figure A5. Individual EDS elemental maps for the 5% LaFe-W-3 sample, where (**a**) Original sample, and distribution maps: (**b**) C, (**c**) O, (**d**) Al, (**e**) Si, (**f**) Ca, (**g**) Fe, (**h**) K, (**i**) La, and (**j**) Mg.

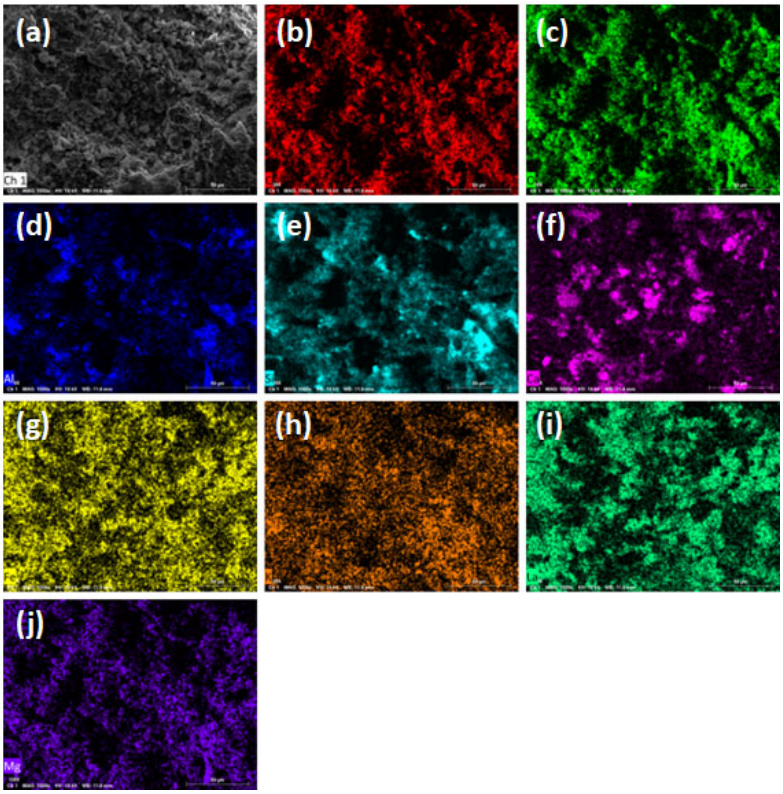

Figure A6. Individual EDS elemental maps for the 5% LaFe-O-3 sample, where (**a**) Original sample, and distribution maps: (**b**) C, (**c**) O, (**d**) Al, (**e**) Si, (**f**) Ca, (**g**) Fe, (**h**) K, (**i**) La, and (**j**) Mg.

References

1. Andrew, R.M. Global CO_2 Emissions from Cement Production, 1928–2018. *Earth Syst. Sci. Data* **2019**, *11*, 1675–1710. [CrossRef]
2. Guo, R.; Wang, J.; Bing, L.; Tong, D.; Ciais, P.; Davis, S.J.; Andrew, R.M.; Xi, F.; Liu, Z. Global CO_2 Uptake by Cement from 1930 to 2019. *Earth Syst. Sci. Data* **2021**, *13*, 1791–1805. [CrossRef]
3. Yang, Y.; Liu, Y.; Liu, L.; Liu, Z.; Wu, H. Monitoring Global Cement Plants from Space. *Remote Sens. Environ.* **2024**, *302*, 113954. [CrossRef]
4. Shyshkin, E.; Chernonosova, T.; Haiko, Y.; Ivasenko, V.; Krasnokutska, I. Recycling of Construction Waste as an Innovative Direction of the Program of Post-War Reconstruction of Destroyed Cities. *Civ. Eng. Pap.* **2023**, *6*, 1039–1047. [CrossRef]
5. Troian, V.; Gots, V.; Flatt, R.J.; Angst, U. Rehabilitating Instead of Rebuilding Aged or Damaged Pre-Fabricated Concrete Buildings for Reducing CO_2 Emissions: The Case of Ukraine. *Mater. Struct.* **2024**, *57*, 14. [CrossRef]
6. Dwivedi, A.; Gupta, S. Carbon Dioxide Sequestration in Mortars with Excavated Soil: Engineering Performances and Environmental Benefits. *Sci. Total Environ.* **2024**, *917*, 170285. [CrossRef]
7. Marsh, A.T.M.; Kulshreshtha, Y. The State of Earthen Housing Worldwide: How Development Affects Attitudes and Adoption. *Build. Res. Inf.* **2022**, *50*, 485–501. [CrossRef]
8. Gallipoli, D.; Bruno, A.W.; Perlot, C.; Mendes, J. A Geotechnical Perspective of Raw Earth Building. *Acta Geotech.* **2017**, *12*, 463–478. [CrossRef]
9. Jaquin, P.A.; Augarde, C.E.; Gallipoli, D.; Toll, D.G. The Strength of Unstabilised Rammed Earth Materials. *Géotechnique* **2009**, *59*, 487–490. [CrossRef]
10. Van Damme, H.; Houben, H. Earth Concrete. Stabilization Revisited. *Cem. Concr. Res.* **2018**, *114*, 90–102. [CrossRef]
11. Hall, M.; Djerbib, Y. Moisture Ingress in Rammed Earth: Part 1—The Effect of Soil Particle-Size Distribution on the Rate of Capillary Suction. *Constr. Build. Mater.* **2004**, *18*, 269–280. [CrossRef]
12. Bui, Q.B.; Morel, J.C.; Venkatarama Reddy, B.V.; Ghayad, W. Durability of Rammed Earth Walls Exposed for 20 Years to Natural Weathering. *Build. Environ.* **2009**, *44*, 912–919. [CrossRef]
13. Guettala, A.; Abibsi, A.; Houari, H. Durability Study of Stabilized Earth Concrete under Both Laboratory and Climatic Conditions Exposure. *Constr. Build. Mater.* **2006**, *20*, 119–127. [CrossRef]
14. Lawson, B. *Building Materials Energy and the Environment: Towards Ecologically Sustainable Development*; Royal Australian Institute of Architects: Red Hill, ACT, Australia, 1996.

15. Alessandrini, G.; Aglietto, M.; Castelvetro, V.; Ciardelli, F.; Peruzzi, R.; Toniolo, L. Comparative Evaluation of Fluorinated and Unfluorinated Acrylic Copolymers as Water-Repellent Coating Materials for Stone. *J. Appl. Polym. Sci.* **2000**, *76*, 962–977. [CrossRef]
16. Toniolo, L.; Poli, T.; Castelvetro, V.; Manariti, A.; Chiantore, O.; Lazzari, M. Tailoring New Fluorinated Acrylic Copolymers as Protective Coatings for Marble. *J. Cult. Herit.* **2002**, *3*, 309–316. [CrossRef]
17. Manoudis, P.N.; Tsakalof, A.; Karapanagiotis, I.; Zuburtikudis, I.; Panayiotou, C. Fabrication of Super-Hydrophobic Surfaces for Enhanced Stone Protection. *Surf. Coat. Technol.* **2009**, *203*, 1322–1328. [CrossRef]
18. Fermo, P.; Cappelletti, G.; Cozzi, N.; Padeletti, G.; Kaciulis, S.; Brucale, M.; Merlini, M. Hydrophobizing Coatings for Cultural Heritage. A Detailed Study of Resin/Stone Surface Interaction. *Appl. Phys. A* **2014**, *116*, 341–348. [CrossRef]
19. Andreotti, S.; Franzoni, E.; Fabbri, P. Poly(Hydroxyalkanoate)s-Based Hydrophobic Coatings for the Protection of Stone in Cultural Heritage. *Materials* **2018**, *11*, 165. [CrossRef]
20. Aslanidou, D.; Karapanagiotis, I.; Lampakis, D. Waterborne Superhydrophobic and Superoleophobic Coatings for the Protection of Marble and Sandstone. *Materials* **2018**, *11*, 585. [CrossRef]
21. Winandy, L.; Schlebusch, O.; Fischer, R. Fungal Hydrophobins Render Stones Impermeable for Water but Keep Them Permeable for Vapor. *Sci. Rep.* **2019**, *9*, 6264. [CrossRef]
22. Sanmartín, P.; Cappitelli, F.; Mitchell, R. Current Methods of Graffiti Removal: A Review. *Constr. Build. Mater.* **2014**, *71*, 363–374. [CrossRef]
23. Macchia, A.; Ruffolo, S.A.; Rivaroli, L.; Malagodi, M.; Licchelli, M.; Rovella, N.; Randazzo, L.; La Russa, M.F. Comparative Study of Protective Coatings for the Conservation of Urban Art. *J. Cult. Herit.* **2020**, *41*, 232–237. [CrossRef]
24. Wolfrum, E.J.; Huang, J.; Blake, D.M.; Maness, P.-C.; Huang, Z.; Fiest, J.; Jacoby, W.A. Photocatalytic Oxidation of Bacteria, Bacterial and Fungal Spores, and Model Biofilm Components to Carbon Dioxide on Titanium Dioxide-Coated Surfaces. *Environ. Sci. Technol.* **2002**, *36*, 3412–3419. [CrossRef] [PubMed]
25. Licciulli, A.; Calia, A.; Lettieri, M.; Diso, D.; Masieri, M.; Franza, S.; Amadelli, R.; Casarano, G. Photocatalytic TiO_2 Coatings on Limestone. *J. Sol-Gel Sci. Technol.* **2011**, *60*, 437–444. [CrossRef]
26. Kapridaki, C.; Maravelaki-Kalaitzaki, P. TiO_2–SiO_2–PDMS Nano-Composite Hydrophobic Coating with Self-Cleaning Properties for Marble Protection. *Prog. Org. Coat.* **2013**, *76*, 400–410. [CrossRef]
27. Bergamonti, L.; Alfieri, I.; Lorenzi, A.; Predieri, G.; Barone, G.; Gemelli, G.; Mazzoleni, P.; Raneri, S.; Bersani, D.; Lottici, P.P. Nanocrystalline TiO_2 Coatings by Sol–Gel: Photocatalytic Activity on Pietra Di Noto Biocalcarenite. *J. Sol-Gel Sci. Technol.* **2015**, *75*, 141–151. [CrossRef]
28. Kapridaki, C.; Pinho, L.; Mosquera, M.J.; Maravelaki-Kalaitzaki, P. Producing Photoactive, Transparent and Hydrophobic SiO_2-Crystalline TiO_2 Nanocomposites at Ambient Conditions with Application as Self-Cleaning Coatings. *Appl. Catal. B Environ.* **2014**, *156–157*, 416–427. [CrossRef]
29. Luo, J.; Cheng, Z.; Yu, N.; Tian, Y.; Meng, J. A Flexible Skin Material with Switchable Wettability for Trans-Medium Vehicles. *Int. J. Smart Nano Mater.* **2025**, *16*, 419–442. [CrossRef]
30. Chen, Y.; Sha, A.; Jiang, W.; Jiao, W.; Cao, Y.; Li, X.; Du, X.; Hu, K.; Lu, Q. Sustainable Thermochromic Coatings for Pavement Cooling and Carbon Offset under Climate Change. *Transp. Res. Part D Transp. Environ.* **2025**, *148*, 104995. [CrossRef]
31. Folli, A.; Strøm, M.; Madsen, T.P.; Henriksen, T.; Lang, J.; Emenius, J.; Klevebrant, T.; Nilsson, Å. Field Study of Air Purifying Paving Elements Containing TiO_2. *Atmos. Environ.* **2015**, *107*, 44–51. [CrossRef]
32. Russell, H.S.; Frederickson, L.B.; Hertel, O.; Ellermann, T.; Jensen, S.S. A Review of Photocatalytic Materials for Urban NO_x Remediation. *Catalysts* **2021**, *11*, 675. [CrossRef]
33. Ghosh, S.; Patra, R.; Majumdar, D.; Sen, K. Developing Scenario of Titania-Based Building Materials for Environmental Remediation. *Int. J. Environ. Sci. Technol.* **2021**, *18*, 2077–2102. [CrossRef]
34. Yang, F.; Takahashi, Y.; Sakai, N.; Tatsuma, T. Visible Light Driven Photocatalysts with Oxidative Energy Storage Abilities. *J. Mater. Chem.* **2011**, *21*, 2288–2293. [CrossRef]
35. Speziale, A.; González-Sánchez, J.F.; Taşcı, B.; Pastor, A.; Sánchez, L.; Fernández-Acevedo, C.; Oroz-Mateo, T.; Salazar, C.; Navarro-Blasco, I.; Fernández, J.M.; et al. Development of Multifunctional Coatings for Protecting Stones and Lime Mortars of the Architectural Heritage. *Int. J. Archit. Herit.* **2020**, *14*, 1008–1029. [CrossRef]
36. Zhao, L.; Xia, M.; Liu, Y.; Zheng, B.; Jiang, Q.; Lian, J. Structure and Photocatalysis of TiO_2/ZnO Double-Layer Film Prepared by Pulsed Laser Deposition. *Mater. Trans.* **2012**, *53*, 463–468. [CrossRef]
37. Reverberi, A.P.; Varbanov, P.S.; Vocciante, M.; Fabiano, B. Bismuth Oxide-Related Photocatalysts in Green Nanotechnology: A Critical Analysis. *Front. Chem. Sci. Eng.* **2018**, *12*, 878–892. [CrossRef]
38. Rani, M.; Keshu; Shanker, U. Efficient Degradation of Organic Pollutants by Novel Titanium Dioxide Coupled Bismuth Oxide Nanocomposite: Green Synthesis, Kinetics and Photoactivity. *J. Environ. Manag.* **2021**, *300*, 113777. [CrossRef]
39. Tena-Santafé, V.M.; Fernández, J.M.; Fernández-Acevedo, C.; Oroz-Mateo, T.; Navarro-Blasco, Í.; Álvarez, J.I. Development of Photocatalytic Coatings for Building Materials with Bi_2O_3-ZnO Nanoparticles. *Catalysts* **2023**, *13*, 1412. [CrossRef]

40. Colangiuli, D.; Lettieri, M.; Masieri, M.; Calia, A. Field Study in an Urban Environment of Simultaneous Self-Cleaning and Hydrophobic Nanosized TiO_2-Based Coatings on Stone for the Protection of Building Surface. *Sci. Total Environ.* **2019**, *650*, 2919–2930. [CrossRef]
41. Kapridaki, C.; Maravelaki, N.-P. TiO_2–SiO_2–PDMS Nanocomposites with Self-Cleaning Properties for Stone Protection and Consolidation. *Geol. Soc. Lond.* **2016**, *416*, 285–292. [CrossRef]
42. La Russa, M.F.; Ruffolo, S.A.; Rovella, N.; Belfiore, C.M.; Palermo, A.M.; Guzzi, M.T.; Crisci, G.M. Multifunctional TiO_2 Coatings for Cultural Heritage. *Prog. Org. Coat.* **2012**, *74*, 186–191. [CrossRef]
43. Tena-Santafé, V.M.; Kyriakou, L.; Oliva, M.d.l.Á.; Sánchez, L.; Fernández, J.M.; Navarro-Blasco, Í.; Álvarez, J.I. Durability and Air-Depolluting Performance of Lime-Based Mortars Treated with Water- and Oil-Repellent Coatings Incorporating Nano-Zn_2TiO_4–ZnO and Nano-$Bi_{12}ZnO_{20}$–ZnO. *Surf. Interfaces* **2025**, *76*, 107879. [CrossRef]
44. Mishra, A.; Priyadarshini, N.; Mansingh, S.; Parida, K. Recent Advancement in $LaFeO_3$-Mediated Systems towards Photocatalytic and Photoelectrocatalytic Hydrogen Evolution Reaction: A Comprehensive Review. *Adv. Colloid Interface Sci.* **2024**, *333*, 103300. [CrossRef] [PubMed]
45. Melo, D.M.A.; Melo, M.A.F.; Martinelli, A.E.; Silva, Z.R.; Cunha, J.D.; Lima, A.C. Synthesis and Characterization of Lanthanum- and Yttrium-Doped Fe_2O_3 Pigments. *Cerâmica* **2007**, *53*, 79–82. [CrossRef]
46. Mishra, M.; Chun, D.-M. α-Fe_2O_3 as a Photocatalytic Material: A Review. *Appl. Catal. A Gen.* **2015**, *498*, 126–141. [CrossRef]
47. Mutter, D.; Urban, D.F.; Elsässer, C. Determination of Formation Energies and Phase Diagrams of Transition Metal Oxides with DFT+U. *Materials* **2020**, *13*, 4303. [CrossRef]
48. Liu, L.; Han, A.; Ye, M.; Zhao, M. Synthesis and Characterization of Al^{3+} Doped $LaFeO_3$ Compounds: A Novel Inorganic Pigments with High near-Infrared Reflectance. *Sol. Energy Mater. Sol. Cells* **2015**, *132*, 377–384. [CrossRef]
49. Coccato, A.; Moens, L.; Vandenabeele, P. On the Stability of Mediaeval Inorganic Pigments: A Literature Review of the Effect of Climate, Material Selection, Biological Activity, Analysis and Conservation Treatments. *Herit. Sci.* **2017**, *5*, 12. [CrossRef]
50. de Jesus Andrade Fidelis, R.; Pires, M.; de Resende, D.S.; Costa Lima, G.F.; de Paiva, P.R.P.; Bezerra, A.C.d.S. Magnetite: Properties and Applications—A Review. *J. Magn. Magn. Mater.* **2025**, *614*, 172770. [CrossRef]
51. Oosterlaken, B.M.; van den Bruinhorst, A.; de With, G. On the Use of Probe Liquids for Surface Energy Measurements. *Langmuir* **2023**, *39*, 16701–16711. [CrossRef]
52. Gao, L.; McCarthy, T.J. A Perfectly Hydrophobic Surface ($\theta_A/\theta_R = 180^\circ/180^\circ$). *J. Am. Chem. Soc.* **2006**, *128*, 9052–9053. [CrossRef] [PubMed]
53. *UNE-EN 15803:2010*; Conservación Del Patrimonio Cultural. Métodos de Ensayo. Determinación de la Permeabilidad al Vapor de Agua (dp). Asociación Española de Normalización (AENOR): Madrid, Spain, 2010.
54. *NISTIR 5078*; National Institute of Standards and Technology. NIST: Gaithersburg, MD, USA, 2018.
55. Hendrickx, R. Using the Karsten Tube to Estimate Water Transport Parameters of Porous Building Materials. *Mater. Struct.* **2013**, *46*, 1309–1320. [CrossRef]
56. Fernández, C.S. Ensayo de Permeabilidad en Fachadas Tubo en L o Tubo RILEM. Patología + Rehabilitación + Construcción. 2012. Available online: https://www.patologiasconstruccion.net/2012/11/ensayo-de-permeabilidad-en-fachadas-tubo-en-l-o-tubo-rilem/ (accessed on 13 April 2026).
57. Cabrera, S.; González, A. Resistencia a Erosión Húmeda en Bloques de Tierra Comprimida. Evaluación de Diferentes Métodos para el Análisis de Resultados. *Rev. Tecnol. Cienc.* **2021**, *40*, 49–62. [CrossRef]
58. Sandoval Alvarado, G.D. Evaluación de la Erosión y la Resistencia del Adobe Adicionado con Cenizas de Carbón y Cal. Bachelor's Thesis, Universidad Católica Santo Toribio de Mogrovejo, Chiclayo, Peru, 2021. Available online: https://repositorio.usat.edu.pe/items/b7278663-cef1-4b5a-b679-f77a538e2341 (accessed on 13 April 2026).
59. Romero Cuentas, V.I.; Callasi Venero, C.D. Estudio Comparativo de Las Propiedades Físico Mecánicas de Las Unidades de Adobe Tradicional Frente a Las Unidades de Adobe Estabilizado Con Asfalto. Bachelor's Thesis, Universidad Andina del Cusco, Cusco, Peru, 2017.
60. *ISO 22197-1:2016(En)*; Fine Ceramics (Advanced Ceramics, Advanced Technical Ceramics)—Test Method for Air-Purification Performance of Semiconducting Photocatalytic Materials—Part 1: Removal of Nitric Oxide. International Organization for Standardization: Geneva, Switzerland, 2016.
61. Pérez-Nicolás, M.; Navarro-Blasco, I.; Fernández, J.M.; Alvarez, J.I. Atmospheric NO_x Removal: Study of Cement Mortars with Iron- and Vanadium-Doped TiO_2 as Visible Light–Sensitive Photocatalysts. *Constr. Build. Mater.* **2017**, *149*, 257–271. [CrossRef]
62. *ISO 14044:2006*; Environmental Management—Life Cycle Assessment—Requirements and Guidelines. International Organization for Standardization: Geneva, Switzerland, 2006.
63. *ISO 15686-5:2017*; Buildings and Constructed Assets—Service Life Planning Part 5: Life-Cycle Costing. International organization for Standardization: Geneva, Switzerland, 2017.
64. Luque Castillo, X.; Yepes, V. Life Cycle Assessment of Social Housing Construction: A Multicriteria Approach. *Build. Environ.* **2025**, *282*, 113294. [CrossRef]

65. Lanthanum Strontium Cobalt Ferrite Cathode Powder. Available online: https://www.fuelcellstore.com/lanthanum-strontium-cobalt-ferrite-cathode-powder?utm_source (accessed on 21 December 2025).
66. Ganguli, R.; Cook, D.R. Rare Earths: A Review of the Landscape. *MRS Energy Sustain.* **2018**, *5*, E9. [CrossRef]
67. Haque, N.; Hughes, A.; Lim, S.; Vernon, C. Rare Earth Elements: Overview of Mining, Mineralogy, Uses, Sustainability and Environmental Impact. *Resources* **2014**, *3*, 614–635. [CrossRef]
68. Blejman, M.G. *Informe Técnico de Huella de Carbono Organizacional CETAQUA 202X*; CETAQUA: Barcelona, Spain, 2021.
69. Greenblatt, J.B.; Miller, D.J.; Ager, J.W.; Houle, F.A.; Sharp, I.D. The Technical and Energetic Challenges of Separating (Photo)Electrochemical Carbon Dioxide Reduction Products. *Joule* **2018**, *2*, 381–420. [CrossRef]
70. Cárdenas-Gómez, J.C.; Gonzales, M.B.; Lazo, C.A.D. Evaluation of Reinforced Adobe Techniques for Sustainable Reconstruction in Andean Seismic Zones. *Sustainability* **2021**, *13*, 4955. [CrossRef]
71. Greenhouse Gas Emission Intensity of Electricity Generation in Europe. Available online: https://www.eea.europa.eu/en/analysis/indicators/greenhouse-gas-emission-intensity-of-1 (accessed on 9 March 2026).
72. Mohammadi, M.; Mohammad, S.M.; Roshanbin, M.; Lomboy, G.R.; Abubakri, S. Advances in Concrete Demolition Technologies: A Review of Conventional and Emerging Methods for Sustainable Waste Management. *Eng* **2024**, *5*, 3174–3191. [CrossRef]
73. Autoline España: Un Mercado en Línea Para Vehículos Comerciales y Recambios. Available online: https://autoline.es/ (accessed on 17 December 2025).
74. Observatorio de Costes Del Transporte de Mercancías | Ministerio de Transportes y Movilidad Sostenible. Available online: https://www.transportes.gob.es/transporte-terrestre/servicios-al-transportista/observatorios-del-transporte/observatorios-del-transporte-de-mercancias-por-carretera/observatorios-costes-transporte-mercancias?utm_source (accessed on 17 December 2025).
75. Renovación, S. Precios de Materiales de Construcción. Available online: https://smartstayrenovation.com/estadisticas/materiales-construccion-precios (accessed on 10 March 2026).
76. Ranganath, S.; McCord, S.; Sick, V. Assessing the Maturity of Alternative Construction Materials and Their Potential Impact on Embodied Carbon for Single-Family Homes in the American Midwest. *Front. Built Environ.* **2024**, *10*, 1384191. [CrossRef]
77. Hammond, G.P.; Jones, C.I. Embodied Energy and Carbon in Construction Materials. *Proc. Inst. Civ. Eng. Energy* **2008**, *161*, 87–98. [CrossRef]
78. Naibaho, M.; Mulyawan, A.; Nehan, P.Z.Z.; Adi, W.A.; Kurniawan, B.; Hung, W.-S.; Widakdo, J.; Ginting, M. Temperature-Dependent Phase Evolution and Reflection Loss of Lanthanum Orthoferrite ($LaFeO_3$). *Inorg. Chem. Commun.* **2025**, *176*, 114246. [CrossRef]
79. Zhang, Q.; Huang, Y.; Peng, S.; Zhang, Y.; Shen, Z.; Cao, J.; Ho, W.; Lee, S.C.; Pui, D.Y.H. Perovskite $LaFeO_3$-$SrTiO_3$ Composite for Synergistically Enhanced NO Removal under Visible Light Excitation. *Appl. Catal. B Environ.* **2017**, *204*, 346–357. [CrossRef]
80. Zhang, Y.; Shen, W.; Li, K.; Li, Y.; Lin, Y. NO_2 Adsorption Behaviors on the Intrinsic, B-Site Doped, and Oxygen Vacancy Defective $LaFeO_3$ (010) Surface. *React. Kinet. Mech. Catal.* **2024**, *137*, 177–193. [CrossRef]
81. Sadrian, M.R.; Calvin, W.M.; McCormack, J. Contrasting Mineral Dust Abundances from X-Ray Diffraction and Reflectance Spectroscopy. *Atmos. Meas. Tech.* **2022**, *15*, 3053–3074. [CrossRef]
82. U.S. Geological Survey. *U.S. Geological Survey Open-File Report 01-041*; U.S. Geological Survey: Reston, VA, USA, 2001. Available online: https://pubs.usgs.gov/of/2001/of01-041/index.htm (accessed on 17 February 2026).
83. Database of Raman Spectroscopy, X-Ray Diffraction and Chemistry of Minerals. Available online: https://rruff.info/ (accessed on 13 November 2025).
84. McCormack, A.; Stone, V.; McQuat, J.; Johnston, H. Investigating the Impact of the Dispersion Protocol on the Physico-Chemical Identity and Toxicity of Nanomaterials: A Review of the Literature with Focus on TiO_2 Particles. *Part. Fibre Toxicol.* **2025**, *22*, 11. [CrossRef]
85. Öztürk, B.; Yavuz, M.; Aydınoğlu, A.; Güven, O.; Hazar, A.B.Y. Effect of Different Drying Techniques on Silaning Efficiency. *Ceram. Int.* **2023**, *49*, 5573–5581. [CrossRef]
86. Miyazawa, T.; Itaya, M.; Burdeos, G.C.; Nakagawa, K.; Miyazawa, T. A Critical Review of the Use of Surfactant-Coated Nanoparticles in Nanomedicine and Food Nanotechnology. *Int. J. Nanomed.* **2021**, *16*, 3937–3999. [CrossRef]
87. Meng, H.; Wang, S.; Xi, J.; Tang, Z.; Jiang, L. Facile Means of Preparing Superamphiphobic Surfaces on Common Engineering Metals. *J. Phys. Chem. C* **2008**, *112*, 11454–11458. [CrossRef]
88. Aydar, A.Y.; Rodriguez-Martinez, V.; Farkas, B.E. Determination and Modeling of Contact Angle of Canola Oil and Olive Oil on a PTFE Surface at Elevated Temperatures Using Air or Steam as Surrounding Media. *LWT* **2016**, *65*, 304–310. [CrossRef]
89. Melo-Espinosa, E.A.; Sánchez-Borroto, Y.; Errasti, M.; Piloto-Rodríguez, R.; Sierens, R.; Roger-Riba, J.; Christopher-Hansen, A. Surface Tension Prediction of Vegetable Oils Using Artificial Neural Networks and Multiple Linear Regression. *Energy Procedia* **2014**, *57*, 886–895. [CrossRef]
90. González Sánchez, A. Obtención de Recubrimientos Superhidrofugantes para Materiales de Construcción, Mediante el Uso de Nanopartículas de Sílice Funcionalizadas. Bachelor's Thesis, Universidad de Cádiz, Cádiz, Spain, 2016.

91. Info-312: Vapor Permeance of Some Building Materials | Buildingscience.com. Available online: https://buildingscience.com/documents/information-sheets/info-312-vapor-permeance-some-materials?utm_source (accessed on 8 April 2026).
92. Narloch, P.; Piątkiewicz, W.; Pietruszka, B. The Effect of Cement Addition on Water Vapour Resistance Factor of Rammed Earth. *Materials* **2021**, *14*, 2249. [CrossRef] [PubMed]
93. *UNE-EN 1504-2:2005*; Productos y Sistemas Para La Protección y Reparación de Estructuras de Hormigón—Parte 2: Revestimientos de Protección. Asociación Española de Normalización: Madrid, Spain, 2005.
94. *DIN 4108-3:2024-03*; Thermal Protection and Energy Economy in Buildings—Part 3: Protection against Moisture Subject to Climate Conditions—Requirements, Calculation Methods and Verification Procedures. Deutsches Institut für Normung: Berlin, Germany, 2024.
95. Calatan, G.; Hegyi, A.; Dico, C.; Mircea, C. Surface waterproofing methods of clay bricks used in vernacular construction. *Int. Multidiscip. Sci. GeoConference (SGEM)* **2015**, *6*, 287–294.
96. Zhang, P.; Wang, Z.; Yin, J.; Wang, M.; Hao, W.; Wen, X.; Wang, B.; Jin, X. Investigation on Aging Behavior and Failure Mechanism of Blast-Resistant Polyurea Coating in Service Environments. *Mater. Today Commun.* **2025**, *44*, 112051. [CrossRef]
97. Pellegrino, F.; Zangirolami, M.; Minero, C.; Maurino, V. Portable Photoreactor for On-Site Measurement of the Activity of Photocatalytic Surfaces. *Catal. Today* **2020**, *340*, 363–368. [CrossRef]
98. Scafetta, M.D.; Cordi, A.M.; Rondinelli, J.M.; May, S.J. Band Structure and Optical Transitions in $LaFeO_3$: Theory and Experiment. *J. Phys. Condens. Matter* **2014**, *26*, 505502. [CrossRef]
99. Ismael, M.; Wark, M. Perovskite-Type $LaFeO_3$: Photoelectrochemical Properties and Photocatalytic Degradation of Organic Pollutants Under Visible Light Irradiation. *Catalysts* **2019**, *9*, 342. [CrossRef]
100. Sora, I.N.; Bertolotti, B.; Pelosato, R.; Lucotti, A.; Tommasini, M.; Muscetta, M. $TiO_2/LaFeO_3$ Composites for the Efficient Degradation of Benzoic Acid and Hydrogen Production. *Molecules* **2025**, *30*, 1526. [CrossRef]